



**HAL**  
open science

## Crystallization of binary nanocrystal superlattices and the relevance of short-range attraction

Emanuele Marino, R. Allen Lacour, Timothy Moore, Sjoerd van Dongen, Austin Keller, Di An, Shengsong Yang, Daniel Rosen, Guillaume Gouget, Esther Tsai, et al.

### ► To cite this version:

Emanuele Marino, R. Allen Lacour, Timothy Moore, Sjoerd van Dongen, Austin Keller, et al.. Crystallization of binary nanocrystal superlattices and the relevance of short-range attraction. *Nature Synthesis*, 2023, 10.1038/s44160-023-00407-2 . hal-04287506

**HAL Id: hal-04287506**

**<https://hal.science/hal-04287506v1>**

Submitted on 20 Nov 2023

**HAL** is a multi-disciplinary open access archive for the deposit and dissemination of scientific research documents, whether they are published or not. The documents may come from teaching and research institutions in France or abroad, or from public or private research centers.

L'archive ouverte pluridisciplinaire **HAL**, est destinée au dépôt et à la diffusion de documents scientifiques de niveau recherche, publiés ou non, émanant des établissements d'enseignement et de recherche français ou étrangers, des laboratoires publics ou privés.

34 *Crystallization of Binary Nanocrystal Superlattices*  
35 *and the Relevance of Short-Ranged Attraction*

36 *Emanuele Marino,<sup>1,8,\*</sup> R. Allen LaCour,<sup>4,\*</sup> Timothy C. Moore,<sup>4</sup> Sjoerd W. van Dongen,<sup>1,6</sup> Austin*  
37 *W. Keller,<sup>2</sup> Di An,<sup>1</sup> Shengsong Yang,<sup>1</sup> Daniel J. Rosen,<sup>2</sup> Guillaume Gouget,<sup>1</sup> Esther H.R. Tsai,<sup>7</sup>*  
38 *Cherie R. Kagan,<sup>1,2,3</sup> Thomas E. Kodger,<sup>6</sup> Sharon C. Glotzer,<sup>4,5,\*</sup> and Christopher B. Murray<sup>1,2,\*</sup>*

39 <sup>1</sup>Department of Chemistry, <sup>2</sup>Department of Materials Science and Engineering, <sup>3</sup>Department of  
40 Electrical and Systems Engineering, University of Pennsylvania. Philadelphia, Pennsylvania,  
41 19104, United States.

42 <sup>4</sup>Department of Chemical Engineering and <sup>5</sup>Biointerfaces Institute, University of Michigan, Ann  
43 Arbor, Michigan 48109, United States.

44 <sup>6</sup>Physical Chemistry and Soft Matter, Wageningen University and Research, 6708WE,  
45 Wageningen, The Netherlands.

46 <sup>7</sup>Brookhaven National Laboratory, Bldg. 735, Center for Functional Nanomaterials, Upton, NY  
47 11973-5000, USA.

48 <sup>8</sup>Dipartimento di Fisica e Chimica, Università degli Studi di Palermo, Via Archirafi 36, 90123  
49 Palermo, Italy.

50

51

## 52 ABSTRACT

53 The synthesis of binary nanocrystal superlattices (BNSLs) enables the targeted integration of  
54 orthogonal physical properties, such as photoluminescence and magnetism, into a single  
55 superstructure, unlocking a vast design space for multifunctional materials. However, the  
56 formation mechanism of BNSLs remains poorly understood, restricting the prediction of the  
57 structure and properties of superlattices. Here, we use a combination of *in situ* scattering and  
58 molecular simulation to elucidate the self-assembly of two common BNSLs ( $\text{AlB}_2$  and  $\text{NaZn}_{13}$ )  
59 through emulsion templating. Our self-assembly experiments reveal that no intermediate structures  
60 precede the formation of the final binary phases, indicating that their formation proceeds through  
61 classical nucleation. Using simulations, we find that, despite the formation of  $\text{AlB}_2$  and  $\text{NaZn}_{13}$   
62 typically being attributed to entropy, their self-assembly is most consistent with the nanocrystals  
63 possessing short-range interparticle attraction, which we find can accelerate nucleation kinetics in  
64 BNSLs. We also find homogenous, classical nucleation in simulation, corroborating our  
65 experiments. These results establish a robust correspondence between experiment and theory,  
66 paving the way towards prediction of BNSLs.

## 67 **Introduction**

68 Recent advances have enabled the synthesis of colloidal nanocrystals (NCs) with different sizes,  
69 shapes, and compositions, generating a library of nanoscale building blocks with well-defined  
70 optical, electronic, and magnetic properties. These properties have been exploited to develop  
71 optoelectronic devices such as photodetectors,<sup>1,2</sup> light-emitting diodes,<sup>3,4</sup> field-effect transistors,<sup>5,6</sup>  
72 and solar cells<sup>7,8</sup> by assembling NCs into ordered solids, or superlattices. While single-component  
73 NC superlattices have already revealed structure-property relationships,<sup>9,10</sup> multi-component NC

74 superlattices are still in the early stages of investigation.<sup>11</sup> The integration of NCs with orthogonal  
75 functionalities is crucial in unlocking a vast synthetic design space for material properties resulting  
76 from the synergistic interaction of the individual components.<sup>12-20</sup> So far, the exploration of this  
77 design space has been restricted by limited understanding of the formation of multi-component  
78 NC superlattices.

79 Binary nanocrystal superlattices (BNSLs) with diverse crystal structures have been synthesized,  
80 integrating combinations of semiconducting, magnetic, and metallic NCs.<sup>21-23</sup> However, predicting  
81 which binary structure assembles from a given combination of NCs has proven challenging.<sup>24</sup> With  
82 rare exceptions,<sup>25-27</sup> simulation models of binary mixtures of NCs frequently fail to self-assemble,  
83 indicating that the current understanding of how NC interactions contribute to the synthesis of  
84 BNSLs is incomplete. By contrast, experimental *in situ* studies have revealed the self-assembly  
85 mechanism of single-component NC superlattices,<sup>28-36</sup> enabling structure prediction by capturing  
86 both kinetic and thermodynamic aspects of how different inter-NC interactions influence  
87 crystallization.<sup>37-43</sup> Yet, in almost two decades since the first observation of BNSLs,<sup>21</sup> only one *in*  
88 *situ* study has focused on mono-functional BNSLs,<sup>44</sup> while no *in situ* studies have investigated the  
89 synthesis of multi-functional BNSLs to our knowledge.

90 Here we combine experiments and simulations to understand the synthesis of multi-functional  
91 BNSLs from a combination of magnetic, semiconducting, and plasmonic NCs. A combination of  
92 magnetic and semiconducting NCs may prove crucial in modulating the temperature of the atomic  
93 lattice and the conductivity of charge carriers,<sup>45,46</sup> and a combination of magnetic and plasmonic  
94 NCs may allow active control over the coherent oscillations of charge carriers and the optical  
95 response of the material.<sup>47,48</sup> We use synchrotron-based *in situ* small-angle X-ray scattering  
96 (SAXS) to follow the real-time self-assembly of BNSLs isostructural to  $\text{AlB}_2$  and  $\text{NaZn}_{13}$ . The

97 NCs were confined to emulsion droplets that were slowly dried to trigger crystallization, resolving  
98 with detail the formation of high-quality BNSLs.<sup>28,49-51</sup> This approach was combined with  
99 molecular dynamics (MD) simulations to determine the interparticle interactions allowing the  
100 formation of these BNSLs. In contrast to some reports of single-component superlattices,<sup>28,30,31,52</sup>  
101 we find that nucleation occurs classically for both superlattices, although significant structural  
102 compression occurs after nucleation, indicating that the ligands are still swollen with solvent at the  
103 time of nucleation. In our MD simulations, we find that, despite the self-assembly of AlB<sub>2</sub> and  
104 NaZn<sub>13</sub> typically being attributed to entropy, only NCs interacting with a short-ranged attraction  
105 between NCs results in self-assembly behavior consistent with experiment. Specifically, we find  
106 that short-range attraction can greatly accelerate the crystallization kinetics of BNSLs. By  
107 establishing a direct link between experiments and simulations, our work provides crucial insights  
108 into the synthesis of BNSLs, providing a significant step towards the targeted synthesis and  
109 structure prediction of these complex, 3D artificial solids.

## 110 **Results and Discussion**

111 We synthesize BNSLs by the self-assembly of binary mixtures of NCs using emulsion-  
112 templating,<sup>49,53</sup> which has recently emerged as a consistent and scalable method to fabricate 3D  
113 single-component NC superlattices.<sup>28,29,53-61</sup> We prepare a surfactant-stabilized oil-in-water  
114 emulsion containing a dispersion of larger (L) super-paramagnetic Fe<sub>3</sub>O<sub>4</sub> and smaller (S)  
115 semiconductor PbS NCs with an effective size ratio of 0.56, a number ratio of 1:2, and a total  
116 inorganic volume fraction of  $\phi = 0.001$ ; see Figures S1-S3 for NC characterization. To collect *in*  
117 *situ* scattering patterns, we flow the emulsion in a closed loop through a quartz capillary aligned  
118 with the X-ray beam; see Figure S4 for a schematic of the setup.<sup>28,57</sup> As the volatile oily phase  
119 evaporates,  $\phi$  increases with time. Figure 1a and Movie S1 illustrate the continuous kinetic

120 evolution of the structure factor,  $S(q)$ . Initially, the structure factor is featureless and centered  
121 around 1, as expected for a colloidal gas. During the first 3 hours of evaporation, broad features  
122 arise across the wave vector range,  $q$ . After 3.6 hours, a succession of sharp peaks suddenly  
123 emerges from the background, growing in intensity while shifting with time towards higher  $q$ . As  
124 highlighted in Figure 1b, the shape of the structure factor at 3.6 hours resembles that of a low-  
125 density colloidal fluid, but within 0.1 hours rapidly develops into a fully formed diffraction pattern  
126 featuring at least 7 sharp peaks from growing crystallites. Immediately thereafter, all peaks shift  
127 synchronously toward higher  $q$ , indicating a contraction of the crystal lattice. We identify the  
128 crystal as isostructural to  $\text{AlB}_2$  with parameters  $a = b \approx c$ ; see Figure 1c. This structure is  
129 characterized by stacked hexagonal layers of the larger NCs intercalated by hexagonal layers of  
130 the smaller NCs that occupy the trigonal prismatic voids left by the larger NCs; see schematic in  
131 Figure S5.

132 To understand the formation of these BNSLs, we extract the evolution of the structural parameters  
133 from *in situ* measurements as shown in Figure 1d. After nucleation, lattice contraction induces a  
134 slow decrease in the surface-to-surface distance between NCs,  $d$ . This decrease takes place over  
135 several hours to reach an inorganic volume fraction of  $\phi = 0.357$ ; see Figure S6. In stark contrast  
136 to this steady compression of the lattice, the average crystal size extracted from the Scherrer  
137 equation,<sup>62</sup>  $\xi$ , increases rapidly: Within 0.1 hours after nucleation, the crystal size increases to  
138 reach  $\xi \approx 330 \text{ nm}$ , corresponding to  $\xi/a \sim 23$  unit cells of the BNSL. Eventually, the crystal size  
139 slowly decreases to  $\xi \approx 280 \text{ nm}$  as the result of lattice compression. Interestingly, we notice that  
140 the integrated intensity of the 001 and 100 reflections grow at different rates relative to the 101  
141 reflection, see Figures 1b-c. While the relative integrated intensity of the 001 reflection increases  
142 by 63% during assembly, that of the 100 reflection increases by 140%, as shown in Figure S7.

143 This suggests a strong tendency of the AlB<sub>2</sub> crystal to grow along the basal plane rather than along  
144 the *c* axis.

145 Based on these observations, we hypothesize the synthetic mechanism shown in the inset of Figure  
146 1d: Crystallization occurs as a single-step transition from the fluid to the crystalline phase. The  
147 relative positions of the diffraction peaks do not change during assembly, implying the absence of  
148 intermediate phases between the fluid and the final crystal. This is a simpler process compared to  
149 previous reports on the synthesis of single-component NC superlattices reporting crystal-to-crystal  
150 transitions.<sup>30,31,52</sup> Crystallization is followed by the continuous compression of the BNSL. We  
151 attribute this compression to the evaporation-driven desorption of solvent from the ligand shell of  
152 the NCs, consistent with reports on single-component systems.<sup>28,30,57</sup> *Ex situ* transmission electron  
153 microscopy (TEM) confirms the synthesis of 3D colloidal BNSLs, each featuring a distinct set of  
154 NC planes, as shown in Figures 1e, S8-S10. The Fourier transform of the BNSL shown in Figure  
155 1e reveals a discrete set of spots, as expected for a crystalline structure. Combining *in situ* and *ex*  
156 *situ* experimental results leads to the structural model shown in Figure 1f. The synthesized BNSLs  
157 retain the superparamagnetic character of their larger NC component, while also displaying a  
158 reduced magnetic remanence and spin density relative to the single-component superlattice, as  
159 shown in Figure S11.

160 We test the robustness of this approach by using a NC pair with comparable size ratio, number  
161 ratio, and initial volume fraction but featuring larger infrared plasmonic CdO NCs co-doped with  
162 fluorine and indium (FICO) and smaller infrared semiconductor PbS NCs (optical activity in  
163 Figure S3). Under the same synthetic conditions, their assembly in emulsion yields the same AlB<sub>2</sub>  
164 BNSL structure with similar kinetics; see Figure S12 and Movie S2. We next target a different  
165 BNSL, NaZn<sub>13</sub>, by increasing the number ratio of these FICO and PbS NCs from 1:2 to 1:13. The

166 experimental structure factor reveals the onset of diffraction peaks from the flat background shortly  
167 after 2.3 hours of drying, as shown in Figure 2a-b and Movie S3. The diffraction pattern appears  
168 qualitatively different from Figure 1, with at least 10 discernible reflections. A more careful  
169 examination of the final diffraction pattern indicates the coexistence of a majority phase  
170 isostructural to  $\text{NaZn}_{13}$  with a minority  $\text{AlB}_2$  phase, as shown in Figure 2c. The  $\text{NaZn}_{13}$  structure  
171 consists of a body-centered icosahedral cluster of 13 smaller particles contained within a simple  
172 cubic subcell of the larger particles, as illustrated in the inset in Figures 2c and S13.

173 We study the synchronous evolution of the  $\text{NaZn}_{13}$  and  $\text{AlB}_2$  phases in Figure 2d. The lattice  
174 parameters of the two crystalline phases slowly decrease as a function of time, to reach maximum  
175 inorganic volume fractions of  $\phi = 0.360$  and  $0.384$  for  $\text{NaZn}_{13}$  and  $\text{AlB}_2$ , respectively. Within 0.1  
176 hours after nucleation, the average domain sizes of the  $\text{NaZn}_{13}$  and  $\text{AlB}_2$  phases rapidly increase  
177 and saturate at their final values of  $\xi \approx 510 \text{ nm}$  and  $200 \text{ nm}$ , respectively. We quantify the fraction  
178 of each crystalline phase by comparing with the assembly performed at a NC number ratio of 1:2,  
179 shown in Figure S12. After nucleation, the fraction of both  $\text{NaZn}_{13}$  and  $\text{AlB}_2$  phases quickly  
180 increases to reach the values of 0.74 and 0.21, respectively, confirming  $\text{NaZn}_{13}$  as the majority  
181 phase. Interestingly, while the fraction of the  $\text{AlB}_2$  phase shows a slow increase in the late stages  
182 of the assembly, that of the  $\text{NaZn}_{13}$  phase shows a comparable decrease. This suggests that even  
183 though the  $\text{NaZn}_{13}$  phase readily nucleates to occupy most of the available volume, this structure  
184 might be thermodynamically less stable than  $\text{AlB}_2$ . The relative strengths of inter-NC interactions  
185 may be responsible for shifting this equilibrium towards one specific phase.

186 *Ex situ* dark-field scanning transmission electron microscopy (STEM) confirms the formation of  
187 3D colloidal  $\text{NaZn}_{13}$  BNSLs; see Figure 2e. The [200] projection clearly illustrates the cubic  
188 symmetry of the  $\text{NaZn}_{13}$  phase, as well as the four-fold symmetry of the smaller NCs surrounding



189 each larger NC; see also Figures S13-S15. In Figure 2f we illustrate a 3D model of this colloidal  
190 BNSL, obtained by carving a sphere out of a  $\text{NaZn}_{13}$  lattice with experimentally determined  
191 structural parameters. We also observe superstructures characterized by a heterostructure of  
192  $\text{NaZn}_{13}$  with a second phase, shown in Figure 2g, confirming the presence of a minority phase as  
193 suggested by SAXS. Due to interference with the adjacent  $\text{NaZn}_{13}$  phase, we are unable to clearly  
194 identify this secondary phase using STEM. However, the results of *in situ* SAXS suggest the  
195 secondary phase should correspond to  $\text{AlB}_2$ .

196 *In situ* measurements draw a detailed picture of the self-assembly process that we juxtapose with  
197 simulations to reveal the driving force behind the synthesis of BNSLs. The formation of  $\text{AlB}_2$  and  
198  $\text{NaZn}_{13}$  BNSLs is frequently attributed to entropy<sup>63,64</sup> because of their high packing fractions<sup>65,66</sup>  
199 and because these are both equilibrium phases of the hard-sphere model,<sup>67</sup> whose phase behavior  
200 is solely dictated by entropy. However, we recently discovered that the self-assembly of the  $\text{AlB}_2$   
201 phase is kinetically prohibited in hard-sphere mixtures at a NC number ratio of 1:2,<sup>68</sup> indicating  
202 that more complex interactions are necessary for its formation.

203 The structure of the resulting BNSLs is largely determined by the effective interactions between  
204 NCs in solution. The NCs used in this work interact through solvent-mediated van der Waals  
205 interactions and superparamagnetic interactions in the case of  $\text{Fe}_3\text{O}_4$  NCs.<sup>69</sup> Although many studies  
206 assume purely repulsive interactions in rationalizing observed phases in BNSLs, the fact that our  
207 experiments find  $\text{AlB}_2$ , yet  $\text{AlB}_2$  does not form from purely repulsive NCs at the number ratio 1:2  
208 used in the experiments, implies attraction cannot be neglected.<sup>68</sup> Examples of NC interaction  
209 potentials with a repulsive core and attractive well have been obtained from atomistic simulations  
210 and theoretical models of similar spheroidal NCs, but the specific shape of the interaction potential  
211 varies among systems.<sup>70-75</sup> We choose to model NC interactions with a Mie potential,<sup>76</sup> which has

212 a repulsive core and an attractive well whose depth and width control the strength and range of  
213 attraction, respectively. To parameterize the potential, we consider the Noro-Frenkel law of  
214 corresponding states,<sup>77</sup> which dictates that only attractive wells with widths above a certain size  
215 will have stable liquid phases in their phase diagram. To compare cases with and without stable  
216 liquid phases, we examine two different well widths, described as “narrow well” and “wide well”,  
217 with widths less than and greater than that size, respectively. We show the narrow and wide well  
218 in Figure 3a-b, scaling the range of the interaction between two NCs by the average of their  
219 effective sizes to account for size differences. For simplicity, the well depth,  $\epsilon$ , is set equal for all  
220 interspecies interactions, that is  $\epsilon_{LL} = \epsilon_{LS} = \epsilon_{SS} = \epsilon$ . While this is an approximation, large  
221 differences in well depths frequently result in demixing,<sup>78</sup> which has been reported for other  
222 experiments on binary nanocrystal self-assembly but not those conducted here. Later, we discuss  
223 the plausible case of  $\epsilon_{LL} > \epsilon_{LS} > \epsilon_{SS}$ , finding similar results to the case of equal attraction strength.  
224 We also examined a case in which the attractive well between the smaller NCs was significantly  
225 narrower than between large NCs, again finding a similar result; see Figure S16.

226 We note that our model assumes that more complex interactions, like many-body or  
227 anisotropic effects, either do not play a large role in determining the phase behavior of these NCs  
228 or they conspire to produce an effective interaction similar to the model. If we detect in simulation  
229 the phases observed in experiment while neglecting these more complex interactions, we can then  
230 infer that the simpler interactions are likely responsible for the formation of these phases.  
231 Furthermore, more complex interactions such as dipolar interactions<sup>79,80</sup> are more likely to be  
232 influenced by the specifics of the NC and solvent compositions, but the AlB<sub>2</sub> and NaZn<sub>13</sub> phases  
233 have been reported for many NC and solvent compositions,<sup>21,22,63,78-82</sup> reducing the likelihood that  
234 composition-dependent interactions are necessary for their self-assembly.

235 To reveal how the range and strength of interaction affect thermodynamic phase behavior,  
236 we compute phase diagrams for a NC number ratio of 1:2, as shown in Figure 3c-d. In the presence  
237 of the narrow well, the gas and solid  $\text{AlB}_2$  phases are both stable. In contrast, in the presence of  
238 the wide well a region of vapor-liquid coexistence is stable above a critical well-depth  $\epsilon_c$ ; see  
239 Figures 3d and S17. This is consistent with the aforementioned Noro-Frenkel law of corresponding  
240 states,<sup>77</sup> which predicts that wider potential wells exhibit a stable liquid–gas transition.

241 While these phase diagrams show the equilibrium predictions for a given set of parameters, they  
242 do not indicate whether a phase is kinetically accessible. To study whether the  $\text{AlB}_2$  phase will  
243 form, we slowly compress an initially disordered fluid under periodic boundary conditions. A  
244 combination of Steinhardt order parameters enables the quantification of the fraction of larger NCs  
245 that become crystalline as a function of time,  $N_{\text{AlB}_2}/N_{\text{Total}}$ ; see Figure S18 for calculation details.<sup>83</sup>  
246 When using a narrow well at least 1.0 kT deep, over 50% of larger NCs crystallize by the end of  
247 the simulations, as shown in Figure 3e. There is limited crystallization for a shallower well of 0.5  
248 kT, and no crystallization when the NCs are purely repulsive. In contrast, only minimal  
249 crystallization occurs with the wide well, with at most 6% of larger NCs registering as crystalline  
250 even for the deepest well investigated, 2.5 kT, as shown in Figure 3f.

251 These results show that a deep, narrow attractive well substantially improves the crystallization  
252 kinetics of  $\text{AlB}_2$ . A similar kinetic enhancement has been reported in simulations of single-  
253 component systems (as discussed below), but to our knowledge this is the first demonstration of  
254 such an effect in a multicomponent system of this nature. Furthermore, the effect is more dramatic  
255 for the case of  $\text{AlB}_2$ , because  $\text{AlB}_2$  fails to crystallize at all without an attractive well but  
256 crystallizes readily with one. In comparable single-component systems, a narrow attractive well

257 can improve crystallization kinetics, but self-assembly still occurs readily without one (i.e. when  
258 the NCs resemble hard spheres).

259 We can rationalize this improvement to kinetics by considering the phase diagrams shown in  
260 Figures 3c-d. In general, crystal nucleation and growth is strongly influenced by the degree of  
261 supersaturation and particle mobility. In the phase diagram shown in Figure 3c, the solid become  
262 stable at low densities (where the particles are highly mobile) for a narrow, deep attractive well. A  
263 similar stabilization of the solid phase occurs for the wide well system, but the dense liquid phase  
264 is also stabilized, reducing the supersaturation. We quantify these effects by computing the  
265 chemical potential driving force between the crystal and fluid phases as a function of NC mobility  
266 in Figure S19, finding that deep, narrow wells do result in higher chemical potential driving forces  
267 at higher particle diffusivities. We also note that this principle of achieving high driving forces at  
268 low density is similar to that proposed for colloids with small attractive patches.<sup>84</sup>

269 To place these observations in a more general context, we investigated the crystallization of two  
270 related systems: a single-component face-centered cubic crystal (FCC) and the two-component  
271 NaZn<sub>13</sub> crystal for the narrow well at different well depths. In Figure S20, we show that, as with  
272 AlB<sub>2</sub>, crystallization of both structures occurs at increasingly lower densities, although for FCC  
273 this shift is not too important because self-assembly still occurs readily without an attractive well.  
274 Furthermore, above its critical well depth, we find that AlB<sub>2</sub> crystallized through a two-step  
275 process in which a dense liquid initially forms; see Figures S21 and S22. This switch to a two-step  
276 nucleation process at the critical point is consistent with previous reports for single-component  
277 systems. Thus, we conclude that crystallization in our binary systems occurs very similarly to that  
278 in single-component systems, except that an attractive force is required to observe the formation  
279 of some binary crystals.

280 In summary, our results indicate that the interaction between NCs during self-assembly is  
281 consistent with a pair potential characterized by a narrow well. We note that such a pair potential  
282 is fairly common for colloids in which vdW forces are the largest contribution to inter-NC  
283 attraction. Furthermore, we note that the narrow attractive well we use closely resembles that used  
284 for similar NCs in a recent study in which the attraction between NCs was assumed to be entirely  
285 vdW interactions between NC cores.<sup>29</sup> We also note that AlB<sub>2</sub> will self-assemble for a broad range  
286 of well depths greater than 0.5 kT, which possibly explains why it self-assembles for a NCs with  
287 different compositions, including the CdO NCs used here.

288  
289 We next checked for further consistency with experiment by simulating conditions closer to  
290 experiment by adding NC polydispersity and spherical confinement to the simulations. We  
291 determine the polydispersity of each NC species by SAXS, Figure S1, and simulate the interaction  
292 of each NC with the confining boundary of the droplet using a Weeks-Chandler-Anderson  
293 potential.<sup>85</sup> Unsurprisingly, we found that adding polydispersity disfavored crystallization, but that  
294 crystallization was still possible on our time scales for the highest well depth examined in Figure  
295 3 (2.5 kT), so we used that well depth in these simulations. Each simulation system is initialized  
296 as a colloidal fluid in a droplet, then slowly compressed to induce self-assembly. In close  
297 agreement with experiment, AlB<sub>2</sub> forms at a NC number ratio of 1:2, while NaZn<sub>13</sub> forms at 1:13.  
298 Interestingly, crystallization begins at a slightly lower volume fraction for NaZn<sub>13</sub> than AlB<sub>2</sub>, 0.528  
299 and 0.572 respectively, as shown in Figure 4a. Simulations performed at lower volume fractions  
300 did not result in self-assembly. As shown by the kinetic change in the fraction of crystalline  
301 particles, rapid crystal growth follows nucleation. Consistent with experiments, we find no  
302 intermediate phases that precede the final phases, indicating classical nucleation from a dense fluid

303 phase.<sup>30,31</sup> Furthermore, we conclude that spherical confinement does not influence the identity of  
304 the self-assembled structure in the systems investigated here.

305  
306 Simulations provide the unparalleled advantage of directly visualizing crystal nucleation,<sup>86-88</sup> a  
307 process notoriously elusive to capture in experiments. The early stages of assembly for NaZn<sub>13</sub>  
308 and AlB<sub>2</sub> BNSLs are shown in Figures 4b and 4c, respectively. To highlight the crystalline nuclei,  
309 we color only the NCs identified as being in a crystalline environment, while fluid-like NCs are  
310 shown as smaller grey spheres. For both NaZn<sub>13</sub> and AlB<sub>2</sub> BNSLs, the critical nuclei emerge from  
311 the fluid multiple particle diameters away from the surface of the droplet, allowing us to conclude  
312 that these BNSLs undergo homogeneous nucleation. Only after nucleation do the crystallites of  
313 NaZn<sub>13</sub> and AlB<sub>2</sub> BNSL spread to the wall. This behavior is unaffected by the size of the droplet,  
314 as shown by replacing the spherical walls with flat walls to simulate significantly larger droplets,  
315 as shown in Figure S23. We find no evidence for exotic pre-nucleation clusters.<sup>63,89</sup>

316 The final stages of growth result in the crystals shown in Figures 4d-e. The NaZn<sub>13</sub> grains are  
317 easily identifiable by the simple cubic arrangement of the larger NCs. A single crystal grain spans  
318 most of the spherical superstructure, consistent with the experimental results shown in Figure 2.  
319 In contrast, multiple grains of AlB<sub>2</sub> are present. This qualitatively agrees with the SAXS  
320 measurements showing smaller grains for AlB<sub>2</sub> than NaZn<sub>13</sub>, although specific crystal grains are  
321 harder to visualize in the TEM micrographs, making a quantitative comparison between simulation  
322 and experiment challenging.

323 An apparent discrepancy remains between experiment and simulation: experimental results  
324 indicate the presence of ~20% AlB<sub>2</sub> as a second phase for samples prepared at a NC number ratio

325 of 1:13, while simulations show less than 1% AlB<sub>2</sub>. Interestingly, reducing the magnitude of the  
326 attraction between smaller NCs results in the coexistence of AlB<sub>2</sub> and NaZn<sub>13</sub> at a NC number  
327 ratio of 1:13, removing the discrepancy as shown in Figure S24. This adjustment is consistent with  
328 the dependence of van der Waals and superparamagnetic interactions on NC size.<sup>90</sup>

## 329 **Conclusions.**

330 We show a remarkable correspondence between experiment and simulation on the synthesis of  
331 BNSLs through self-assembly. While early efforts using evaporation-driven self-assembly have  
332 revealed the tendency to nucleate multiple polymorphs simultaneously,<sup>22,79,91-93</sup> our results show  
333 that emulsion-templated assembly provides a more controlled pathway towards the generation of  
334 phase-pure BNSLs. Under spherical confinement, NCs readily nucleate into binary phases  
335 isostructural to AlB<sub>2</sub> and NaZn<sub>13</sub> without intermediate liquid or crystal phases. The burst of crystal  
336 nucleation is followed by a gradual lattice contraction to result in multifunctional, 3D, dense,  
337 crystalline binary phases. We can accurately reproduce these experimental results in simulation by  
338 introducing a short-ranged, attractive potential which kinetically promotes self-assembly. This  
339 direct link between experiments and simulations reveals that BNSLs nucleate homogeneously and  
340 directly, without intermediate solid phases preceding the final crystal. Aspects of our results likely  
341 apply to NCs coated with DNA-based ligands,<sup>40,94-96</sup> which may provide more continuous control  
342 over the range of interactions and thus allow for a more direct probing of the remaining open  
343 questions. In achieving a closer correspondence between experiment and simulation, and  
344 demonstrating the importance of short-range attraction for assembly kinetics, this work represents  
345 a crucial first step in prediction of BNSLs towards the deterministic hetero-integration of NCs into  
346 multifunctional structures, targeting applications in photonics,<sup>53,58-60,97-99</sup> excitonics,<sup>58,100</sup>  
347 phononics,<sup>101,102</sup> and catalysis.<sup>103,104</sup>

## 348 **Methodology**

### 349 *Experiments*

350 **Synthesis and characterization of the NC building blocks:** Oleate-functionalized PbS (lead  
351 sulfide, rock-salt structure,  $4.5 \pm 0.4$  nm and  $6.4 \pm 0.6$  nm in diameter), Fe<sub>3</sub>O<sub>4</sub> (iron oxide, cubic  
352 spinel structure,  $10.4 \pm 0.6$  nm in diameter), and FICO (fluorine and indium co-doped cadmium  
353 oxide, rock-salt structure,  $13.2 \pm 0.9$  nm in diameter) NCs were synthesized by following reported  
354 procedures and redispersed in toluene.<sup>103,105,106</sup> The NC concentration was determined either by  
355 spectrophotometry by using a published sizing curve<sup>107</sup> (PbS, Figure S3) or by weighing the dry  
356 pellet (Fe<sub>3</sub>O<sub>4</sub> and FICO). The size of the inorganic cores of the NCs was determined by fitting the  
357 SAXS pattern measured from a dilute dispersion of NCs with a spherical form factor, Figure S1.  
358 The form factor was convoluted with a Gaussian distribution of sizes to account for NC  
359 polydispersity. The fitting was performed by using the free software SASfit.<sup>108</sup> The effective size  
360 of the NCs was determined by imaging a monolayer of NCs by TEM, calculating the fast-Fourier  
361 transform of the image, and extracting the center-to-center distance between nearest neighbors,  
362 Figure S2. A complete description of these procedures is available in the supplementary  
363 information.

364 ***In situ* SAXS:** The kinetic patterns were collected at the SMI beamline, Brookhaven National  
365 Laboratory, using a recently developed experimental setup.<sup>28</sup> To conserve beamtime, we expanded  
366 the setup to support the simultaneous measurement of 4 samples by translating the sample stage  
367 vertically; see schematic in Figure S4. Each sample was prepared as follows: A 20 mL scintillation  
368 vial was charged with 8 mL of 200 mM sodium dodecyl sulfate in water. Subsequently, the vial  
369 was charged with 2 mL of a NC dispersion in 22 v/v % toluene and 78 v/v % hexanes with a total



370 NC volume fraction of 0.001. The vial was capped and vigorously vortexed for 60 seconds using  
371 a vortex mixer (Fisher) to generate the emulsion. The emulsion was then uncapped and diluted by  
372 adding 10 mL of 200 mM sodium dodecyl sulfate in water. A 1-inch octagonal stir bar was then  
373 added to the diluted emulsion. The vial was placed on a hotplate (IKA plate) equipped with a  
374 thermocouple and a heating block for vials, heated to 70 °C while stirring at 500 rpm, and allowed  
375 to flow by means of a peristaltic pump (Cole-Palmer) at a flow rate of 10 mL min<sup>-1</sup> through a  
376 closed loop of Viton peristaltic tubing (Cole-Palmer). The closed loop included a custom-made  
377 flow cell consisting of a 1 mm quartz capillary tube (Charles Supper). The X-ray beam was aligned  
378 with the center of the capillary. This setup allowed us to measure the scattering pattern from the  
379 emulsion as evaporation occurred from the uncapped vial. The integration time for each  
380 measurement was set to 1 second, the time between consecutive acquisitions was 28 seconds, the  
381 beam energy was 16.1 keV, and the sample to detector distance was 6.3 meters. The q-range was  
382 calibrated against a silver behenate standard. The two-dimensional patterns were azimuthally  
383 averaged, and background subtracted to yield  $I(q, t)$ , where  $t$  is the time. The kinetic structure  
384 factor,  $S(q, t)$ , was then obtained by calculating  $S(q, t) = I(q, t)/I(q, 0)$  since at the beginning of  
385 the experiment the NCs are well dispersed within the droplets.

386 **Structural parameters of AlB<sub>2</sub>:** For a hexagonal structure (Figure S5), the expected reflections  
387  $q_{hkl}$  for the planes of indexes  $hkl$  are:

388 
$$q_{hkl} = \sqrt{\frac{4h^2 + hk + k^2}{3a^2} + \frac{l^2}{c^2}}$$

389 We first extracted the  $c/a$  factor for the AlB<sub>2</sub> structure for the last data point,  $t = t_{end}$ . We did so  
390 empirically by generating the expected positions  $q_{hkl}$  of the reflections for a given value of  $c/a$ ,

391 and comparing with the experimental results until an agreement was found. We found that the  
 392 value of  $c/a$  does not vary as the structure evolves during drying. To calculate the kinetic structural  
 393 parameters, we first fitted each  $S(q, t)$  curve with a superposition of Lorentzian curves with line  
 394 shape:

$$395 \quad L(q) = \frac{Aw^2}{(q - q_{hkl})^2 + w^2}$$

396 centered around the expected  $q_{hkl}$  positions, with amplitude  $A$  and full width at half maximum  
 397  $2w$ . Since  $q_{101}$  was the most isolated reflection, we used it to calculate the kinetic structural  
 398 parameters. From the Scherrer equation, we calculated the average crystal size as  $\xi = 2\pi K/2w =$   
 399  $\pi K/w$ , where  $K = 1.0747$  is the Scherrer constant used for a spherical crystal.<sup>109</sup> The lattice  
 400 parameter, also equal to the center-to-center distance, or bond length, between larger (L) NCs was  
 401 calculated as:

$$402 \quad b_{LL} = a = \frac{2\pi}{q_{101}} \sqrt{\frac{4}{3} + \frac{1}{(c/a)^2}}$$

403 The surface-to-surface distance between larger NCs was then calculated as  $d_{LL} = b_{LL} - \sigma_L$ , where  
 404  $\sigma_L$  is the average diameter of the inorganic cores of the larger NCs as measured by *ex situ* SAXS.  
 405 The bond length between smaller (S) NCs was calculated by scaling by the expected values for the  
 406 bond lengths in the atomic  $\text{AlB}_2$  structure for which  $b_{LL,At} = 0.30090 \text{ nm}$  and  $b_{SS,At} =$   
 407  $0.17372 \text{ nm}$  so that  $b_{SS} = b_{LL}(b_{SS,At}/b_{LL,At})$ . The surface-to-surface distance between smaller  
 408 NCs was then calculated as  $d_{SS} = b_{SS} - \sigma_S$ , where  $\sigma_S$  is the average diameter of the inorganic  
 409 cores of the smaller NCs as measured by *ex situ* SAXS. The bond length between larger and smaller  
 410 NCs was then calculated as  $b_{LS} = b_{LL}(b_{LS,At}/b_{LL,At})$ , where  $b_{LS,At}$  is the bond length in the atomic

411 AlB<sub>2</sub> structure for measured value of  $c/a$  in the nanocrystal superstructure. For  $c/a = 0.99$ ,  
 412  $b_{AB,At} = 0.22883 \text{ nm}$ . The surface-to-surface distance between larger and smaller NCs was then  
 413 determined as  $d_{LS} = b_{LS} - \sigma_L/2 - \sigma_S/2$ . Additional details are provided in the supporting  
 414 information.

415 **Structural parameters of NaZn<sub>13</sub>**: For a cubic structure (Figure S13), the expected reflections  
 416  $q_{hkl}$  for the planes of indexes  $hkl$  are:

$$417 \quad q_{hkl} = \frac{2\pi}{a} \sqrt{h^2 + k^2 + l^2}$$

418 To calculate the kinetic structural parameters, we first fitted each  $S(q, t)$  curve with a  
 419 superposition of Lorentzian curves with line shape centered around the expected  $q_{hkl}$  positions,  
 420 with amplitude  $A$  and full width at half maximum  $2w$ . Since  $q_{200}$  was the most isolated reflection,  
 421 we used it to calculate the kinetic structural parameters. From the Scherrer equation, we calculated  
 422 the average crystal size as  $\xi = \pi K/w$ . The lattice parameter  $a$ , twice the center-to-center distance,  
 423 or bond length, between larger NCs,  $b_{LL}$ , was calculated as  $2b_{LL} = a = 4\pi/q_{200}$ . The surface-to-  
 424 surface distance between larger NCs was then calculated as  $d_{LL} = b_{LL} - \sigma_L$ . The bond length  
 425 between smaller NCs was calculated by scaling by the expected values for the bond lengths in the  
 426 atomic NaZn<sub>13</sub> structure for which  $b_{LL,At} = 0.61365 \text{ nm}$  and  $b_{SS,At} = 0.25664 \text{ nm}$  so that  $b_{SS} =$   
 427  $b_{LL}(b_{SS,At}/b_{LL,At})$ . The surface-to-surface distance between smaller NCs was then calculated as  
 428  $d_{SS} = b_{SS} - \sigma_S$ . The bond length between larger and smaller NCs was then calculated as  $b_{LS} =$   
 429  $b_{LL}(b_{LS,At}/b_{LL,At})$  where  $b_{LS,At} = 0.35647 \text{ nm}$  is the bond length in the atomic NaZn<sub>13</sub> structure.  
 430 The surface-to-surface distance between larger and smaller NCs was then determined as  $d_{LS} =$   
 431  $b_{LS} - \sigma_L/2 - \sigma_S/2$ . Additional details are provided in the supporting information.

432 **Electron microscopy:** For TEM and STEM imaging, a JEOL F200 microscope was operated at  
 433 200 kV. During imaging, magnification, focus and tilt angle were varied to yield information about  
 434 the crystal structure and super structure of the particle systems. To prepare the superstructures for  
 435 imaging, after the emulsion had fully dried, the binary NC superstructures were washed twice in a  
 436 solution of 20 mM sodium dodecyl sulfate in water by centrifugation at 3000 g for 30 minutes,  
 437 and redispersed. 10  $\mu$ L of the dispersion was drop casted on a carbon-coated TEM grid (EMS) and  
 438 dried under vacuum for 1 hour. The grid was then dipped in a cleaning solution consisting of 1:2  
 439 water:isopropanol by volume, and dried for 1 hour under vacuum.

440 **Rendering:** The coordinates for a three-dimensional superlattice with parameters matching  
 441 experiment were initially generated by using a self-developed script. A sphere of a desired size  
 442 matching a superstructure was then carved from the superlattice. The positions and sizes of all  
 443 particles were then sent to the free software Blender 2.93 and rendered.

#### 444 *Simulations*

445 We used molecular dynamics (MD) with the HOOMD-Blue simulation toolkit<sup>110</sup> to simulate a  
 446 binary mixture of NCs with interactions modeled by the Mie (IPL) potential:

$$447 \quad U_{ij}(r_{ij}) = \varepsilon_{ij} \left( \frac{n}{n-m} \right) \left( \frac{n}{m} \right)^{\frac{m}{n-m}} \left( \left( \frac{\sigma_{ij}}{r_{ij}} \right)^n - \left( \frac{\sigma_{ij}}{r_{ij}} \right)^m \right)$$

448 where  $U_{ij}(r_{ij})$  is the energy between two NCs (particles)  $i$  and  $j$  separated by a distance  $r_{ij}$ . The  
 449 potential is described by four parameters: a measure of the particle's size,  $\sigma_{ij}$ ; the power of the  
 450 repulsive component,  $n$ ; the magnitude of the interaction,  $\varepsilon_{ij}$ ; and the length scale of the attractive  
 451 interaction,  $m$ . We set  $\sigma_{ij}$  to match the effective size ratio of the NCs used in experiment:  $\sigma_{SS} =$

452  $0.55 * \sigma_{LL}$ ,  $\sigma_{LS} = \frac{0.55+1}{2} * \sigma_{LL}$ , and  $\sigma_{LL} = 1$ , where  $L$  represents the larger NCs and  $S$  the smaller  
453 NCs. For simplicity, we set the depth of the potential well to be equal for all particle pairs:  $\epsilon_{LL} =$   
454  $\epsilon_{LS} = \epsilon_{SS} = \epsilon$ . We also use  $\sigma$  to represent  $\sigma_{LL}$  in the text. For consistency with previous works,<sup>68</sup>  
455 we set the power  $n$  to a value of 50. We analyze systems with  $m$  of 6 and 25, which we refer to as  
456 “wide well” and “narrow well” respectively. The resulting potentials are shown in Figure 3a-b for  
457 a well-depth of 1.0 kT. Throughout the paper we manipulate the well depth by changing the  
458 temperature, which is inversely proportional to the well depth. We define the units of time as  $\tau =$   
459  $\sigma \left( \frac{w}{\epsilon} \right)^{\frac{1}{2}}$ , where  $w$  is mass and set to 1 for every type of particle. For  $\epsilon/kT = 0$  shown in Figure 3c-  
460 d, we simulated an inverse power law potential at 1.0 kT, similarly to previous work.<sup>68</sup>

461 To compute the free energies of different phases in Figure 3c and 3d, we combined thermodynamic  
462 integration with the Einstein molecule method,<sup>111</sup> a variant of the Frenkel-Ladd method,<sup>112</sup> using  
463 at least 2,000 particles in every case. The free energies of the gas and liquid phases were computed  
464 at a stoichiometry of 1:2. Self-assembly was attempted with 27,000 particles by slowly  
465 compressing the particles from an initially disordered fluid state to a crystalline or kinetically  
466 arrested amorphous state. In Figure S25 we give the range of densities compressed over for each  
467 well depth and width. We also compute the diffusion coefficient in the vicinity of kinetic arrest.  
468 We used NVT simulations based on the MTK equations<sup>113</sup> to thermostat our simulations in Figure  
469 3e-f and NVT simulations using a Langevin integrator<sup>114</sup> to thermostat our simulations in Figure  
470 4.

471 For the simulations in Figure 4, we treat the distribution of particle sizes as a mixture of two normal  
472 distributions: one centered at a size of  $1\sigma_{LL}$  and one centered at a size of  $0.55\sigma_{LL}$ . The standard  
473 deviations ( $s$ ) of the normal distributions were chosen to match experiment:  $s = 0.047\sigma_{LL}$  for that

474 of the larger particles and  $s = 0.063\sigma_{ss}$  for that of the smaller particles. We then discretized the  
475 distributions, with 13 bins associated with each peak. We placed the particles inside a spherical  
476 droplet, whose edges repel the particles with a Weeks-Chandler-Anderson potential.<sup>85</sup> We  
477 computed an effective packing fraction by calculating an effective particle size according to the  
478 prescription of Barker and Henderson.<sup>115</sup> We scaled the wall's range of interaction by  $\sigma_i/2$ , which  
479 accounts for the different sizes of the particles.

480 We used Steinhardt order parameters<sup>83</sup> in Figures 3 and 4 to identify crystalline particles. The  
481 specific combinations for each crystal are shown in Figure S18. The parameters were calculated  
482 using the *freud* software library.<sup>116</sup> In Figure S22 we used the local density of each particle to infer  
483 the occurrence of two-step nucleation. We computed the local density using the implementation  
484 provided by *freud*<sup>116</sup>, in which the contribution of each neighbor is scaled by the interparticle  
485 distance and diameter of the particle. We used  $r_{max} = 1.3\sigma$  and a diameter of  $1.0\sigma$  in the calculation.  
486 We classified particles as locally dense if the local density was greater than  $1.05/\sigma^3$ ,  $1.6/\sigma^3$ , and  
487  $2.5/\sigma^3$  for simulations of FCC, AlB<sub>2</sub>, and NaZn<sub>13</sub>, respectively. These cutoffs were chosen to  
488 separate particles belonging to the initial low-density fluid phase from denser fluid and crystal  
489 phases.

490 We used Ovito<sup>117</sup> to visualize our simulations throughout this work.

491 The computational workflow and data management for this publication was primarily supported  
492 by the *signac* data management framework.<sup>118,119</sup>

493

494 DATA AVAILABILITY

495 The authors declare that the data supporting the findings of this study are available within the  
496 article and its supplementary information files. Source data for the figures in the main text are  
497 available as supporting information.

498

#### 499 CODE AVAILABILITY

500 The source code for HOOMD-blue is available at <https://github.com/glotzerlab/hoomd-blue>. The  
501 source code for freud is available at <https://github.com/glotzerlab/freud>. The source code for  
502 signac is available at <https://github.com/glotzerlab/signac>. Source data for the figures in the main  
503 text are available as supporting information. Sample codes are available as supporting  
504 information.

505

#### 506 ACKNOWLEDGMENT

507 The authors acknowledge primary support from the National Science Foundation under Grant  
508 DMR-2019444. E.M. and S.Y. acknowledge support from the Office of Naval Research  
509 Multidisciplinary University Research Initiative Award ONR N00014-18-1-2497 for sample  
510 preparation and characterization. E.M. is grateful to the National Recovery and Resilience Plan  
511 (NRRP) PNR 2021-2022 (CUP B79J21038330001) for funding his position at Unipa. E.M.  
512 acknowledges the Fondo Finalizzato Alla Ricerca Di Ateneo (FFR) 2022-2023 of Unipa for  
513 funding. A.W.K. and C.R.K. acknowledge support from the Semiconductor Research Corporation  
514 (SRC) under the Nanomanufacturing Materials and Processes (NMP) trust via Task 2797.001.  
515 D.J.R. acknowledges support from the VIEST fellowship. G.G. acknowledges Solvay for financial  
516 support. C.B.M. acknowledges the Richard Perry University Professorship at the University of  
517 Pennsylvania. Support for the Dual Source and Environmental X-ray Scattering Facility at the

518 University of Pennsylvania was provided by the Laboratory for Research on the Structure of  
519 Matter which is funded in part by NSF MRSEC 1720530. This research used resources of the  
520 Center for Functional Nanomaterials and the National Synchrotron Light Source II, which are U.S.  
521 DOE Office of Science Facilities, at Brookhaven National Laboratory under Contract No.  
522 DESC0012704. Computational work used resources from the Extreme Science and Engineering  
523 Discovery Environment (XSEDE),<sup>120</sup> which is supported by National Science Foundation grant  
524 number ACI-1548562; XSEDE Award DMR 140129. Additional computational resources and  
525 services supported by Advanced Research Computing at the University of Michigan, Ann Arbor.

526

## 527 AUTHOR INFORMATION

### 528 **Corresponding Author**

529 \*email: cbmurray@sas.upenn.edu, sglotzer@umich.edu

### 530 **Author Contributions**

531 E.M. designed the experiment. E.M., S.W.v.D., A.W.K., and D.A. synthesized and characterized  
532 the NC building blocks. E.M., S.W.v.D., S.Y., D.J.R., and E.H.R.T. measured the *in situ* scattering  
533 data. E.M. analyzed the results. E.H.R.T. provided local support at the beamline. E.M., G.G., and  
534 S.W.v.D. performed the electron microscopy studies. D.J.R. performed the magnetic  
535 measurements. R.A.L. and T.C.M. performed the simulations and analyzed the results. T.E.K.,  
536 S.C.G., C.R.K, and C.B.M. supervised the project. The manuscript was written through  
537 contributions of all authors. All authors have given approval to the final version of the manuscript.

538 \*These authors contributed equally.

539



540 COMPETING INTERESTS

541 The authors declare no competing interests.

542

543 FIGURE CAPTIONS

544 **Figure 1:** Formation of colloidal  $\text{AlB}_2$  binary nanocrystal superlattices (BNSLs). (a) Kinetic  
545 structure factor,  $S(q)$ , of a binary dispersion of PbS and  $\text{Fe}_3\text{O}_4$  nanocrystals (NCs) under spherical  
546 confinement of a drying emulsion. (b)  $S(q)$  patterns showing the emergence and evolution of  
547 diffraction peaks around the time of BNSL nucleation. (c) Final  $S(q)$  pattern identifying the BNSL  
548 structure as  $\text{AlB}_2$ . The inset shows the unit cell of  $\text{AlB}_2$ . (d) Evolution of the crystalline lattice after  
549 nucleation, highlighting the kinetics of surface-to-surface distance,  $d$ , between larger (L) and  
550 smaller (S) NCs, and average crystal size  $\xi$ . (e) Transmission electron micrograph of PbS and  
551  $\text{Fe}_3\text{O}_4$  NCs crystallized into a three-dimensional  $\text{AlB}_2$  BNSL. The fast-Fourier transform is shown  
552 as inset. (f) Model of the  $\text{AlB}_2$  BNSL shown in (e). Figure key: blue and pink spheres are used to  
553 indicate the larger and smaller NCs in the mixture

554

555 **Figure 2:** Formation of colloidal  $\text{NaZn}_{13}$  binary nanocrystal superlattices (BNSLs). (a) Kinetic  
556 structure factor,  $S(q)$ , of a binary dispersion of PbS and FICO nanocrystals (NCs) under spherical  
557 confinement of a drying emulsion. (b)  $S(q)$  patterns showing the emergence and evolution of  
558 diffraction peaks around the time of BNSL nucleation. (c) Final  $S(q)$  pattern identifying the BNSL  
559 structure as  $\text{NaZn}_{13}$  with a minority  $\text{AlB}_2$  phase. The inset shows the sub-unit cell of  $\text{NaZn}_{13}$ . (d)  
560 Evolution of the surface-to-surface distance,  $d$ , between larger (L) and smaller (S) NCs, average  
561 crystal size  $\xi$ , and phase fraction of  $\text{NaZn}_{13}$  and  $\text{AlB}_2$  phases during lattice compression. (e) Dark-  
562 field scanning transmission electron micrograph of a single-crystal  $\text{NaZn}_{13}$  BNSL, and (f) its

563 structural model. (g) Dark-field scanning transmission electron micrograph of a heterostructure  
564 showing the coexistence of  $\text{NaZn}_{13}$  with a secondary phase. Figure key: The blue and pink spheres  
565 are used to represent the larger and smaller NCs.

566

567 **Figure 3:** The influence of attractive forces in binary mixtures. (a-b) Mie pair potentials shown as  
568 a function of the normalized interparticle distance,  $U(r/\sigma)$ , calculated for a well depth of 1 kT and  
569 for length scale parameters  $m = 25$  (a) and  $m = 6$  (b). The potential in (a) is described as the  
570 “narrow well” and the one in (b) as the “wide well” in the main text. For each potential, three types  
571 of interactions are shown: between larger (LL) nanocrystals (NCs), between larger and smaller  
572 (LS) NCs, and between smaller (SS) NCs. (c-d) Thermodynamic phase diagrams computed from  
573 free energy calculations for the narrow (c) and wide well (d) as a function of well depth,  $\epsilon$ , and  
574 normalized particle density,  $\rho\sigma^3$ . The blue and orange lines demarcate the regions of gas-solid  
575 coexistence and vapor-liquid coexistence, respectively. Errors in the phase boundaries are smaller  
576 than the points. The dashed red line in (d) indicates the critical well depth  $\epsilon_c$  above which vapor-  
577 liquid coexistence occurs. The phase diagrams are computed at a NC number ratio of 1:2. (e-f)  
578 The evolution of the number of  $\text{AlB}_2$ -like particles in self-assembly simulations through slow  
579 compression for the narrow (e) and wide well (f).

580

581 **Figure 4:** The self-assembly of  $\text{AlB}_2$  and  $\text{NaZn}_{13}$  in spherical droplets. In (a) we show the results  
582 of attempts to self-assemble  $\text{AlB}_2$  and  $\text{NaZn}_{13}$  with the deepest (2.5 kT), narrow well used in Figure  
583 3. The curve labelled “ $\text{NaZn}_{13}$ ” was obtained at a stoichiometry of 1:13, while the curve labelled  
584 “ $\text{AlB}_2$ ” was obtained at a stoichiometry of 1:2;  $N_{\text{crys}}/N_{\text{total}}$  is the fraction of large particles we  
585 identify as  $\text{NaZn}_{13}$ -like or  $\text{AlB}_2$ -like respectively. In (b) and (c) we show early stages of the

586 growing NaZn<sub>13</sub> and AlB<sub>2</sub> crystals, respectively. We show two different time points, (i) and (ii);  
587 the color of the images' borders match that of the corresponding timepoints in (a) from which they  
588 were taken. We show large particles identified as crystalline in blue and small particles  
589 neighboring a crystalline large particle in pink; all other particles are reduced in size and colored  
590 grey. In (d) and (e), we visualize an inner slice of each droplet at the final time point of our  
591 simulations, coloring every particle. Unlike the simulations in Figure 3, each species is set to have  
592 the polydispersity of the corresponding experimental nanoparticles.

593

594

## 595 REFERENCES

- 596 1 Konstantatos, G. *et al.* Ultrasensitive solution-cast quantum dot photodetectors. *Nature*  
597 **442**, 180-183, doi:10.1038/nature04855 (2006).
- 598 2 Tang, X., Ackerman, M. M., Chen, M. & Guyot-Sionnest, P. Dual-band infrared imaging  
599 using stacked colloidal quantum dot photodiodes. *Nature Photonics* **13**, 277-282,  
600 doi:10.1038/s41566-019-0362-1 (2019).
- 601 3 Caruge, J. M., Halpert, J. E., Wood, V., Bulović, V. & Bawendi, M. G. Colloidal  
602 quantum-dot light-emitting diodes with metal-oxide charge transport layers. *Nature*  
603 *Photonics* **2**, 247-250, doi:10.1038/nphoton.2008.34 (2008).
- 604 4 Kim, T. *et al.* Efficient and stable blue quantum dot light-emitting diode. *Nature* **586**,  
605 385-389, doi:10.1038/s41586-020-2791-x (2020).
- 606 5 Talapin, D. V. & Murray, C. B. PbSe Nanocrystal Solids for n- and p-Channel Thin Film  
607 Field-Effect Transistors. *Science* **310**, 86, doi:10.1126/science.1116703 (2005).
- 608 6 Zhao, Q. *et al.* Enhanced Carrier Transport in Strongly Coupled, Epitaxially Fused CdSe  
609 Nanocrystal Solids. *Nano Letters* **21**, 3318-3324, doi:10.1021/acs.nanolett.1c00860  
610 (2021).
- 611 7 Luther, J. M. *et al.* Schottky Solar Cells Based on Colloidal Nanocrystal Films. *Nano*  
612 *Letters* **8**, 3488-3492, doi:10.1021/nl802476m (2008).
- 613 8 Swarnkar, A. *et al.* Quantum dot-induced phase stabilization of  $\alpha$ -CsPbI<sub>3</sub> perovskite for  
614 high-efficiency photovoltaics. *Science* **354**, 92-95, doi:10.1126/science.aag2700 (2016).
- 615 9 Lan, X. *et al.* Quantum dot solids showing state-resolved band-like transport. *Nature*  
616 *Materials* **19**, 323-329, doi:10.1038/s41563-019-0582-2 (2020).
- 617 10 Mueller, N. S. *et al.* Deep strong light-matter coupling in plasmonic nanoparticle  
618 crystals. *Nature* **583**, 780-784, doi:10.1038/s41586-020-2508-1 (2020).
- 619 11 Cherniukh, I. *et al.* Perovskite-type superlattices from lead halide perovskite nanocubes.  
620 *Nature* **593**, 535-542, doi:10.1038/s41586-021-03492-5 (2021).

- 621 12 Urban, J. J., Talapin, D. V., Shevchenko, E. V., Kagan, C. R. & Murray, C. B. Synergism  
622 in binary nanocrystal superlattices leads to enhanced p-type conductivity in self-  
623 assembled PbTe/Ag<sub>2</sub>Te thin films. *Nature Materials* **6**, 115-121, doi:10.1038/nmat1826  
624 (2007).
- 625 13 Chen, J. *et al.* Collective Dipolar Interactions in Self-Assembled Magnetic Binary  
626 Nanocrystal Superlattice Membranes. *Nano Letters* **10**, 5103-5108,  
627 doi:10.1021/nl103568q (2010).
- 628 14 Chen, J. *et al.* Bistable Magnetoresistance Switching in Exchange-Coupled CoFe<sub>2</sub>O<sub>4</sub>-  
629 Fe<sub>3</sub>O<sub>4</sub> Binary Nanocrystal Superlattices by Self-Assembly and Thermal Annealing. *ACS*  
630 *Nano* **7**, 1478-1486, doi:10.1021/nn3052617 (2013).
- 631 15 Dong, A., Chen, J., Ye, X., Kikkawa, J. M. & Murray, C. B. Enhanced Thermal Stability  
632 and Magnetic Properties in NaCl-Type FePt-MnO Binary Nanocrystal Superlattices.  
633 *Journal of the American Chemical Society* **133**, 13296-13299, doi:10.1021/ja2057314  
634 (2011).
- 635 16 Kang, Y. *et al.* Design of Pt-Pd Binary Superlattices Exploiting Shape Effects and  
636 Synergistic Effects for Oxygen Reduction Reactions. *Journal of the American Chemical*  
637 *Society* **135**, 42-45, doi:10.1021/ja3097527 (2013).
- 638 17 Kang, Y. *et al.* Engineering Catalytic Contacts and Thermal Stability: Gold/Iron Oxide  
639 Binary Nanocrystal Superlattices for CO Oxidation. *Journal of the American Chemical*  
640 *Society* **135**, 1499-1505, doi:10.1021/ja310427u (2013).
- 641 18 Zhang, M. *et al.* High-strength magnetically switchable plasmonic nanorods assembled  
642 from a binary nanocrystal mixture. *Nature Nanotechnology* **12**, 228-232,  
643 doi:10.1038/nnano.2016.235 (2017).
- 644 19 Cargnello, M. *et al.* Substitutional doping in nanocrystal superlattices. *Nature* **524**, 450-  
645 453, doi:10.1038/nature14872 (2015).
- 646 20 Lee, J.-S., Kovalenko, M. V., Huang, J., Chung, D. S. & Talapin, D. V. Band-like  
647 transport, high electron mobility and high photoconductivity in all-inorganic nanocrystal  
648 arrays. *Nature Nanotechnology* **6**, 348-352, doi:10.1038/nnano.2011.46 (2011).
- 649 21 Redl, F. X., Cho, K. S., Murray, C. B. & O'Brien, S. Three-dimensional binary  
650 superlattices of magnetic nanocrystals and semiconductor quantum dots. *Nature* **423**,  
651 968-971, doi:10.1038/nature01702 (2003).
- 652 22 Shevchenko, E. V., Talapin, D. V., Kotov, N. A., O'Brien, S. & Murray, C. B. Structural  
653 diversity in binary nanoparticle superlattices. *Nature* **439**, 55-59,  
654 doi:10.1038/nature04414 (2006).
- 655 23 Kiely, C. J., Fink, J., Brust, M., Bethell, D. & Schiffrin, D. J. Spontaneous ordering of  
656 bimodal ensembles of nanoscopic gold clusters. *Nature* **396**, 444-446, doi:10.1038/24808  
657 (1998).
- 658 24 Heil, C. M. & Jayaraman, A. Computational Reverse-Engineering Analysis for Scattering  
659 Experiments of Assembled Binary Mixture of Nanoparticles. *ACS Materials Au* **1**, 140-  
660 156, doi:10.1021/acsmaterialsau.1c00015 (2021).
- 661 25 Bommineni, P. K., Klement, M. & Engel, M. Spontaneous Crystallization in Systems of  
662 Binary Hard Sphere Colloids. *Physical Review Letters* **124**, 218003,  
663 doi:10.1103/PhysRevLett.124.218003 (2020).
- 664 26 Wang, D. *et al.* Binary icosahedral clusters of hard spheres in spherical confinement.  
665 *Nature Physics* **17**, 128-134, doi:10.1038/s41567-020-1003-9 (2021).

- 666 27 Coli, G. M. & Dijkstra, M. An Artificial Neural Network Reveals the Nucleation  
667 Mechanism of a Binary Colloidal AB<sub>13</sub> Crystal. *ACS Nano* **15**, 4335-4346,  
668 doi:10.1021/acsnano.0c07541 (2021).
- 669 28 Marino, E., Kodger, T. E., Wegdam, G. H. & Schall, P. Revealing Driving Forces in  
670 Quantum Dot Supercrystal Assembly. **30**, 1803433,  
671 doi:<https://doi.org/10.1002/adma.201803433> (2018).
- 672 29 Montanarella, F. *et al.* Crystallization of Nanocrystals in Spherical Confinement Probed  
673 by in Situ X-ray Scattering. *Nano Letters* **18**, 3675-3681,  
674 doi:10.1021/acs.nanolett.8b00809 (2018).
- 675 30 Weidman, M. C., Smilgies, D.-M. & Tisdale, W. A. Kinetics of the self-assembly of  
676 nanocrystal superlattices measured by real-time in situ X-ray scattering. *Nature Materials*  
677 **15**, 775-781, doi:10.1038/nmat4600 (2016).
- 678 31 Geuchies, J. J. *et al.* In situ study of the formation mechanism of two-dimensional  
679 superlattices from PbSe nanocrystals. *Nature Materials* **15**, 1248-1254,  
680 doi:10.1038/nmat4746 (2016).
- 681 32 Abécassis, B., Testard, F. & Spalla, O. Gold Nanoparticle Superlattice Crystallization  
682 Probed In Situ. *Physical Review Letters* **100**, 115504,  
683 doi:10.1103/PhysRevLett.100.115504 (2008).
- 684 33 Narayanan, S., Wang, J. & Lin, X.-M. Dynamical Self-Assembly of Nanocrystal  
685 Superlattices during Colloidal Droplet Evaporation by in situ Small Angle X-Ray  
686 Scattering. *Physical Review Letters* **93**, 135503, doi:10.1103/PhysRevLett.93.135503  
687 (2004).
- 688 34 Connolly, S., Fullam, S., Korgel, B. & Fitzmaurice, D. Time-Resolved Small-Angle X-  
689 ray Scattering Studies of Nanocrystal Superlattice Self-Assembly. *Journal of the*  
690 *American Chemical Society* **120**, 2969-2970, doi:10.1021/ja974273e (1998).
- 691 35 Yu, Y., Yu, D., Sadigh, B. & Orme, C. A. Space- and time-resolved small angle X-ray  
692 scattering to probe assembly of silver nanocrystal superlattices. *Nature Communications*  
693 **9**, 4211, doi:10.1038/s41467-018-06734-9 (2018).
- 694 36 Wu, L. *et al.* High-temperature crystallization of nanocrystals into three-dimensional  
695 superlattices. *Nature* **548**, 197-201, doi:10.1038/nature23308 (2017).
- 696 37 Gong, J. *et al.* Shape-dependent ordering of gold nanocrystals into large-scale  
697 superlattices. *Nature Communications* **8**, 14038, doi:10.1038/ncomms14038 (2017).
- 698 38 Lin, H. *et al.* Clathrate colloidal crystals. *Science* **355**, 931, doi:10.1126/science.aal3919  
699 (2017).
- 700 39 Yue, K. *et al.* Geometry induced sequence of nanoscale Frank–Kasper and quasicrystal  
701 mesophases in giant surfactants. *Proceedings of the National Academy of Sciences* **113**,  
702 14195, doi:10.1073/pnas.1609422113 (2016).
- 703 40 Macfarlane, R. J. *et al.* Nanoparticle Superlattice Engineering with DNA. *Science* **334**,  
704 204, doi:10.1126/science.1210493 (2011).
- 705 41 Tang, Z., Zhang, Z., Wang, Y., Glotzer, S. C. & Kotov, N. A. Self-Assembly of CdTe  
706 Nanocrystals into Free-Floating Sheets. *Science* **314**, 274, doi:10.1126/science.1128045  
707 (2006).
- 708 42 Leunissen, M. E. *et al.* Ionic colloidal crystals of oppositely charged particles. *Nature*  
709 **437**, 235-240, doi:10.1038/nature03946 (2005).
- 710 43 Wang, T. *et al.* Self-Assembled Colloidal Superparticles from Nanorods. *Science* **338**,  
711 358-363, doi:10.1126/science.1224221 (2012).

712 44 Lu, C., Akey, A. J., Dahlman, C. J., Zhang, D. & Herman, I. P. Resolving the Growth of  
713 3D Colloidal Nanoparticle Superlattices by Real-Time Small-Angle X-ray Scattering.  
714 *Journal of the American Chemical Society* **134**, 18732-18738, doi:10.1021/ja307848h  
715 (2012).

716 45 Rosen, D. J., Yang, S., Marino, E., Jiang, Z. & Murray, C. B. In Situ EXAFS-Based  
717 Nanothermometry of Heterodimer Nanocrystals under Induction Heating. *The Journal of*  
718 *Physical Chemistry C* **126**, 3623-3634, doi:10.1021/acs.jpcc.2c00608 (2022).

719 46 Rosen, D. J. *et al.* Microwave Heating of Nanocrystals for Rapid, Low-Aggregation  
720 Intermetallic Phase Transformations. *ACS Materials Letters* **4**, 823-830,  
721 doi:10.1021/acsmaterialslett.2c00174 (2022).

722 47 Yang, S. *et al.* Self-Assembly of Atomically Aligned Nanoparticle Superlattices from Pt-  
723 Fe<sub>3</sub>O<sub>4</sub> Heterodimer Nanoparticles. *Journal of the American Chemical Society* **145**, 6280-  
724 6288, doi:10.1021/jacs.2c12993 (2023).

725 48 Gabbani, A. *et al.* Magnetoplasmonics beyond Metals: Ultrahigh Sensing Performance in  
726 Transparent Conductive Oxide Nanocrystals. *Nano Letters* **22**, 9036-9044,  
727 doi:10.1021/acs.nanolett.2c03383 (2022).

728 49 Velev Orlin, D., Lenhoff Abraham, M. & Kaler Eric, W. A Class of Microstructured  
729 Particles Through Colloidal Crystallization. *Science* **287**, 2240-2243,  
730 doi:10.1126/science.287.5461.2240 (2000).

731 50 Wang, P.-p., Qiao, Q., Zhu, Y. & Ouyang, M. Colloidal Binary Supracrystals with  
732 Tunable Structural Lattices. *Journal of the American Chemical Society* **140**, 9095-9098,  
733 doi:10.1021/jacs.8b05643 (2018).

734 51 Kister, T., Mravlak, M., Schilling, T. & Kraus, T. Pressure-controlled formation of  
735 crystalline, Janus, and core-shell supraparticles. *Nanoscale* **8**, 13377-13384,  
736 doi:10.1039/C6NR01940D (2016).

737 52 Abelson, A. *et al.* Collective topo-epitaxy in the self-assembly of a 3D quantum dot  
738 superlattice. *Nature Materials* **19**, 49-55, doi:10.1038/s41563-019-0485-2 (2020).

739 53 Marino, E. *et al.* Monodisperse Nanocrystal Superparticles through a Source-Sink  
740 Emulsion System. *Chemistry of Materials* **34**, 2779-2789,  
741 doi:10.1021/acs.chemmater.2c00039 (2022).

742 54 Lacava, J., Born, P. & Kraus, T. Nanoparticle Clusters with Lennard-Jones Geometries.  
743 *Nano Letters* **12**, 3279-3282, doi:10.1021/nl3013659 (2012).

744 55 de Nijs, B. *et al.* Entropy-driven formation of large icosahedral colloidal clusters by  
745 spherical confinement. *Nature Materials* **14**, 56-60, doi:10.1038/nmat4072 (2015).

746 56 Wintzheimer, S. *et al.* Supraparticles: Functionality from Uniform Structural Motifs. *ACS*  
747 *Nano* **12**, 5093-5120, doi:10.1021/acsnano.8b00873 (2018).

748 57 Marino, E. *et al.* Favoring the Growth of High-Quality, Three-Dimensional Supercrystals  
749 of Nanocrystals. *The Journal of Physical Chemistry C* **124**, 11256-11264,  
750 doi:10.1021/acs.jpcc.0c02805 (2020).

751 58 Marino, E. *et al.* Simultaneous Photonic and Excitonic Coupling in Spherical Quantum  
752 Dot Supercrystals. *ACS Nano* **14**, 13806-13815, doi:10.1021/acsnano.0c06188 (2020).

753 59 Savo, R. *et al.* Broadband Mie driven random quasi-phase-matching. *Nature Photonics*  
754 **14**, 740-747, doi:10.1038/s41566-020-00701-x (2020).

755 60 Montanarella, F. *et al.* Lasing Supraparticles Self-Assembled from Nanocrystals. *ACS*  
756 *Nano* **12**, 12788-12794, doi:10.1021/acsnano.8b07896 (2018).

757 61 Tang, Y. *et al.* Highly Stable Perovskite Supercrystals via Oil-in-Oil Templating. *Nano*  
758 *Letters* **20**, 5997-6004, doi:10.1021/acs.nanolett.0c02005 (2020).

759 62 Patterson, A. L. The Scherrer Formula for X-Ray Particle Size Determination. *Physical*  
760 *Review* **56**, 978-982, doi:10.1103/PhysRev.56.978 (1939).

761 63 Bodnarchuk, M. I., Kovalenko, M. V., Heiss, W. & Talapin, D. V. Energetic and  
762 Entropic Contributions to Self-Assembly of Binary Nanocrystal Superlattices:  
763 Temperature as the Structure-Directing Factor. *Journal of the American Chemical Society*  
764 **132**, 11967-11977, doi:10.1021/ja103083q (2010).

765 64 Yang, Z., Wei, J. & Pileni, M.-P. Metal–Metal Binary Nanoparticle Superlattices: A Case  
766 Study of Mixing Co and Ag Nanoparticles. *Chemistry of Materials* **27**, 2152-2157,  
767 doi:10.1021/acs.chemmater.5b00123 (2015).

768 65 Murray, M. J. & Sanders, J. V. Close-packed structures of spheres of two different sizes  
769 II. The packing densities of likely arrangements. *Philosophical Magazine A* **42**, 721-740,  
770 doi:10.1080/01418618008239380 (1980).

771 66 Chen, Z. & O’Brien, S. Structure Direction of II–VI Semiconductor Quantum Dot Binary  
772 Nanoparticle Superlattices by Tuning Radius Ratio. *ACS Nano* **2**, 1219-1229,  
773 doi:10.1021/nm800129s (2008).

774 67 Eldridge, M. D., Madden, P. A. & Frenkel, D. Entropy-driven formation of a superlattice  
775 in a hard-sphere binary mixture. *Nature* **365**, 35-37, doi:10.1038/365035a0 (1993).

776 68 LaCour, R. A., Moore, T. C. & Glotzer, S. C. Tuning Stoichiometry to Promote  
777 Formation of Binary Colloidal Superlattices. *Physical Review Letters* **128**, 188001,  
778 doi:10.1103/PhysRevLett.128.188001 (2022).

779 69 Bishop, K. J. M., Wilmer, C. E., Soh, S. & Grzybowski, B. A. Nanoscale Forces and  
780 Their Uses in Self-Assembly. *Small* **5**, 1600-1630,  
781 doi:<https://doi.org/10.1002/sml.200900358> (2009).

782 70 Schapotschnikow, P., Pool, R. & Vlucht, T. J. H. Molecular Simulations of Interacting  
783 Nanocrystals. *Nano Letters* **8**, 2930-2934, doi:10.1021/nl8017862 (2008).

784 71 Liepold, C., Smith, A., Lin, B., de Pablo, J. & Rice, S. A. Pair and many-body  
785 interactions between ligated Au nanoparticles. *The Journal of Chemical Physics* **150**,  
786 044904, doi:10.1063/1.5064545 (2019).

787 72 Baran, Ł. & Sokołowski, S. Effective interactions between a pair of particles modified  
788 with tethered chains. *The Journal of Chemical Physics* **147**, 044903,  
789 doi:10.1063/1.4994919 (2017).

790 73 Munaò, G., Correa, A., Pizzirusso, A. & Milano, G. On the calculation of the potential of  
791 mean force between atomistic nanoparticles. *The European Physical Journal E* **41**, 38,  
792 doi:10.1140/epje/i2018-11646-3 (2018).

793 74 Kaushik, A. P. & Clancy, P. Solvent-driven symmetry of self-assembled nanocrystal  
794 superlattices—A computational study. *Journal of Computational Chemistry* **34**, 523-532,  
795 doi:<https://doi.org/10.1002/jcc.23152> (2013).

796 75 Kister, T., Monego, D., Mulvaney, P., Widmer-Cooper, A. & Kraus, T. Colloidal  
797 Stability of Apolar Nanoparticles: The Role of Particle Size and Ligand Shell Structure.  
798 *ACS Nano* **12**, 5969-5977, doi:10.1021/acs.nano.8b02202 (2018).

799 76 Mie, G. Zur kinetischen Theorie der einatomigen Körper. *Annalen der Physik* **316**, 657-  
800 697, doi:<https://doi.org/10.1002/andp.19033160802> (1903).

801 77 Noro, M. G. & Frenkel, D. Extended corresponding-states behavior for particles with  
802 variable range attractions. *The Journal of Chemical Physics* **113**, 2941-2944,  
803 doi:10.1063/1.1288684 (2000).

804 78 Coropceanu, I., Boles, M. A. & Talapin, D. V. Systematic Mapping of Binary  
805 Nanocrystal Superlattices: The Role of Topology in Phase Selection. *Journal of the*  
806 *American Chemical Society* **141**, 5728-5740, doi:10.1021/jacs.8b12539 (2019).

807 79 Shevchenko, E. V., Talapin, D. V., Murray, C. B. & O'Brien, S. Structural  
808 Characterization of Self-Assembled Multifunctional Binary Nanoparticle Superlattices.  
809 *Journal of the American Chemical Society* **128**, 3620-3637, doi:10.1021/ja0564261  
810 (2006).

811 80 Yang, Z., Wei, J., Bonville, P. & Pileni, M.-P. Beyond Entropy: Magnetic Forces Induce  
812 Formation of Quasicrystalline Structure in Binary Nanocrystal Superlattices. *Journal of*  
813 *the American Chemical Society* **137**, 4487-4493, doi:10.1021/jacs.5b00332 (2015).

814 81 Evers, W. H. *et al.* Entropy-Driven Formation of Binary Semiconductor-Nanocrystal  
815 Superlattices. *Nano Letters* **10**, 4235-4241, doi:10.1021/nl102705p (2010).

816 82 Boles, M. A. & Talapin, D. V. Many-Body Effects in Nanocrystal Superlattices:  
817 Departure from Sphere Packing Explains Stability of Binary Phases. *Journal of the*  
818 *American Chemical Society* **137**, 4494-4502, doi:10.1021/jacs.5b00839 (2015).

819 83 Steinhardt, P. J., Nelson, D. R. & Ronchetti, M. Bond-orientational order in liquids and  
820 glasses. *Physical Review B* **28**, 784-805, doi:10.1103/PhysRevB.28.784 (1983).

821 84 Romano, F., Sanz, E. & Sciortino, F. Crystallization of tetrahedral patchy particles in  
822 silico. *The Journal of Chemical Physics* **134**, 174502, doi:10.1063/1.3578182 (2011).

823 85 Weeks, J. D., Chandler, D. & Andersen, H. C. Role of Repulsive Forces in Determining  
824 the Equilibrium Structure of Simple Liquids. *The Journal of Chemical Physics* **54**, 5237-  
825 5247, doi:10.1063/1.1674820 (1971).

826 86 Moroni, D., ten Wolde, P. R. & Bolhuis, P. G. Interplay between Structure and Size in a  
827 Critical Crystal Nucleus. *Physical Review Letters* **94**, 235703,  
828 doi:10.1103/PhysRevLett.94.235703 (2005).

829 87 Rein ten Wolde, P., Ruiz-Montero, M. J. & Frenkel, D. Numerical calculation of the rate  
830 of crystal nucleation in a Lennard-Jones system at moderate undercooling. *The Journal of*  
831 *Chemical Physics* **104**, 9932-9947, doi:10.1063/1.471721 (1996).

832 88 Zimmermann, N. E. R., Vorselaars, B., Quigley, D. & Peters, B. Nucleation of NaCl from  
833 Aqueous Solution: Critical Sizes, Ion-Attachment Kinetics, and Rates. *Journal of the*  
834 *American Chemical Society* **137**, 13352-13361, doi:10.1021/jacs.5b08098 (2015).

835 89 Gebauer, D., Völkel, A. & Cölfen, H. Stable Prenucleation Calcium Carbonate Clusters.  
836 *Science* **322**, 1819-1822, doi:10.1126/science.1164271 (2008).

837 90 Israelachvili, J. N. *Intermolecular and surface forces*. (Academic press, 2015).

838 91 Shevchenko, E. V., Talapin, D. V., O'Brien, S. & Murray, C. B. Polymorphism in AB13  
839 Nanoparticle Superlattices: An Example of Semiconductor–Metal Metamaterials.  
840 *Journal of the American Chemical Society* **127**, 8741-8747, doi:10.1021/ja050510z  
841 (2005).

842 92 Ye, X., Chen, J. & Murray, C. B. Polymorphism in Self-Assembled AB6 Binary  
843 Nanocrystal Superlattices. *Journal of the American Chemical Society* **133**, 2613-2620,  
844 doi:10.1021/ja108708v (2011).



845 93 Chen, J., Ye, X. & Murray, C. B. Systematic Electron Crystallographic Studies of Self-  
846 Assembled Binary Nanocrystal Superlattices. *ACS Nano* **4**, 2374-2381,  
847 doi:10.1021/nn1003259 (2010).

848 94 Park, S. Y. *et al.* DNA-programmable nanoparticle crystallization. *Nature* **451**, 553-556,  
849 doi:10.1038/nature06508 (2008).

850 95 Nykypanchuk, D., Maye, M. M., van der Lelie, D. & Gang, O. DNA-guided  
851 crystallization of colloidal nanoparticles. *Nature* **451**, 549-552, doi:10.1038/nature06560  
852 (2008).

853 96 Lu, F., Yager, K. G., Zhang, Y., Xin, H. & Gang, O. Superlattices assembled through  
854 shape-induced directional binding. *Nature Communications* **6**, 6912,  
855 doi:10.1038/ncomms7912 (2015).

856 97 Marino, E., Bharti, H., Xu, J., Kagan, C. R. & Murray, C. B. Nanocrystal Superparticles  
857 with Whispering-Gallery Modes Tunable through Chemical and Optical Triggers. *Nano*  
858 *Letters*, doi:10.1021/acs.nanolett.2c01011 (2022).

859 98 Kumar, P. *et al.* Photonically active bowtie nanoassemblies with chirality continuum.  
860 *Nature* **615**, 418-424, doi:10.1038/s41586-023-05733-1 (2023).

861 99 Neuhaus, S. J., Marino, E., Murray, C. B. & Kagan, C. R. Frequency Stabilization and  
862 Optically Tunable Lasing in Colloidal Quantum Dot Superparticles. *Nano Letters* **23**,  
863 645-651, doi:10.1021/acs.nanolett.2c04498 (2023).

864 100 Vanmaekelbergh, D. *et al.* Shape-Dependent Multiexciton Emission and Whispering  
865 Gallery Modes in Supraparticles of CdSe/Multishell Quantum Dots. *ACS Nano* **9**, 3942-  
866 3950, doi:10.1021/nn507310f (2015).

867 101 Poyser, C. L. *et al.* Coherent Acoustic Phonons in Colloidal Semiconductor Nanocrystal  
868 Superlattices. *ACS Nano* **10**, 1163-1169, doi:10.1021/acsnano.5b06465 (2016).

869 102 Bozyigit, D. *et al.* Soft surfaces of nanomaterials enable strong phonon interactions.  
870 *Nature* **531**, 618-622, doi:10.1038/nature16977 (2016).

871 103 Voznyy, O. *et al.* Machine Learning Accelerates Discovery of Optimal Colloidal  
872 Quantum Dot Synthesis. *ACS Nano* **13**, 11122-11128, doi:10.1021/acsnano.9b03864  
873 (2019).

874 104 Guntern, Y. T. *et al.* Synthetic Tunability of Colloidal Covalent Organic  
875 Framework/Nanocrystal Hybrids. *Chemistry of Materials* **33**, 2646-2654,  
876 doi:10.1021/acs.chemmater.1c00501 (2021).

877 105 Park, J. *et al.* Ultra-large-scale syntheses of monodisperse nanocrystals. *Nature Materials*  
878 **3**, 891-895, doi:10.1038/nmat1251 (2004).

879 106 Ye, X., Fei, J., Diroll, B. T., Paik, T. & Murray, C. B. Expanding the Spectral Tunability  
880 of Plasmonic Resonances in Doped Metal-Oxide Nanocrystals through Cooperative  
881 Cation–Anion Codoping. *Journal of the American Chemical Society* **136**, 11680-11686,  
882 doi:10.1021/ja5039903 (2014).

883 107 Moreels, I. *et al.* Size-Dependent Optical Properties of Colloidal PbS Quantum Dots.  
884 *ACS Nano* **3**, 3023-3030, doi:10.1021/nn900863a (2009).

885 108 Bressler, I., Kohlbrecher, J. & Thunemann, A. F. SASfit: a tool for small-angle scattering  
886 data analysis using a library of analytical expressions. *Journal of Applied*  
887 *Crystallography* **48**, 1587-1598, doi:doi:10.1107/S1600576715016544 (2015).

888 109 Langford, J. I. & Wilson, A. J. C. Scherrer after sixty years: A survey and some new  
889 results in the determination of crystallite size. *Journal of Applied Crystallography* **11**,  
890 102-113, doi:doi:10.1107/S0021889878012844 (1978).

891 110 Anderson, J. A., Glaser, J. & Glotzer, S. C. HOOMD-blue: A Python package for high-  
892 performance molecular dynamics and hard particle Monte Carlo simulations.  
893 *Computational Materials Science* **173**, 109363,  
894 doi:<https://doi.org/10.1016/j.commatsci.2019.109363> (2020).

895 111 Noya, E. G., Conde, M. M. & Vega, C. Computing the free energy of molecular solids by  
896 the Einstein molecule approach: Ices XIII and XIV, hard-dumbbells and a patchy model  
897 of proteins. *The Journal of Chemical Physics* **129**, 104704, doi:10.1063/1.2971188  
898 (2008).

899 112 Frenkel, D. & Ladd, A. J. C. New Monte Carlo method to compute the free energy of  
900 arbitrary solids. Application to the fcc and hcp phases of hard spheres. *The Journal of*  
901 *Chemical Physics* **81**, 3188-3193, doi:10.1063/1.448024 (1984).

902 113 Martyna, G. J., Tobias, D. J. & Klein, M. L. Constant pressure molecular dynamics  
903 algorithms. *The Journal of Chemical Physics* **101**, 4177-4189, doi:10.1063/1.467468  
904 (1994).

905 114 Phillips, C. L., Anderson, J. A. & Glotzer, S. C. Pseudo-random number generation for  
906 Brownian Dynamics and Dissipative Particle Dynamics simulations on GPU devices.  
907 *Journal of Computational Physics* **230**, 7191-7201,  
908 doi:<https://doi.org/10.1016/j.jcp.2011.05.021> (2011).

909 115 Barker, J. A. & Henderson, D. What is "liquid"? Understanding the states of matter.  
910 *Reviews of Modern Physics* **48**, 587-671, doi:10.1103/RevModPhys.48.587 (1976).

911 116 Ramasubramani, V. *et al.* freud: A software suite for high throughput analysis of particle  
912 simulation data. *Computer Physics Communications* **254**, 107275,  
913 doi:<https://doi.org/10.1016/j.cpc.2020.107275> (2020).

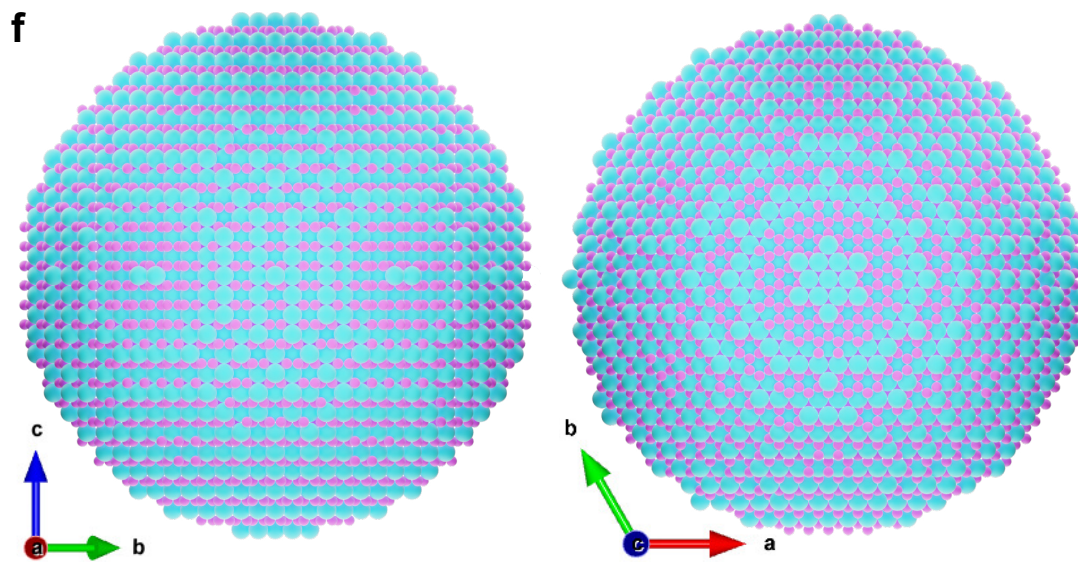
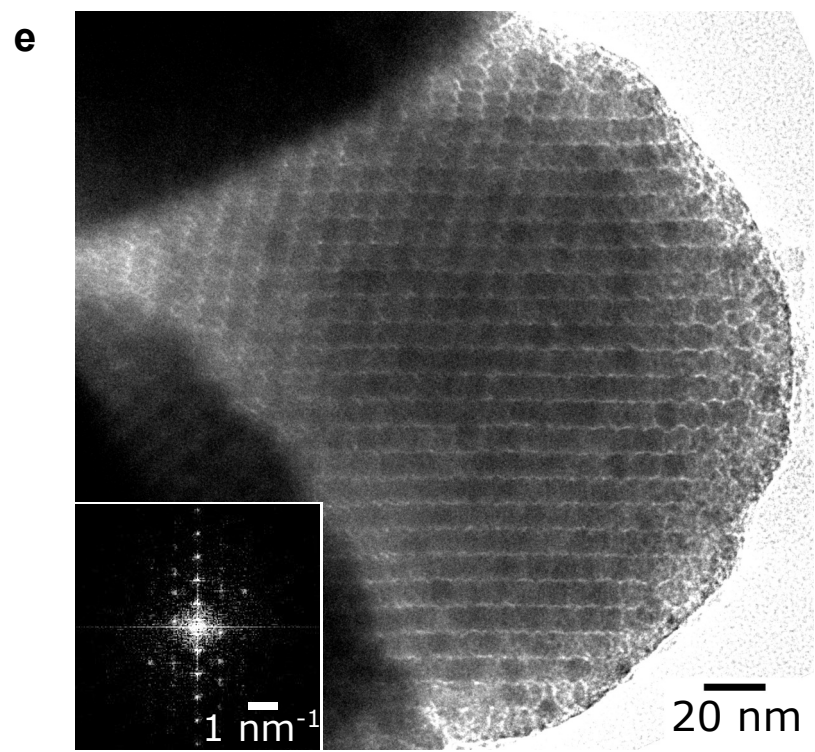
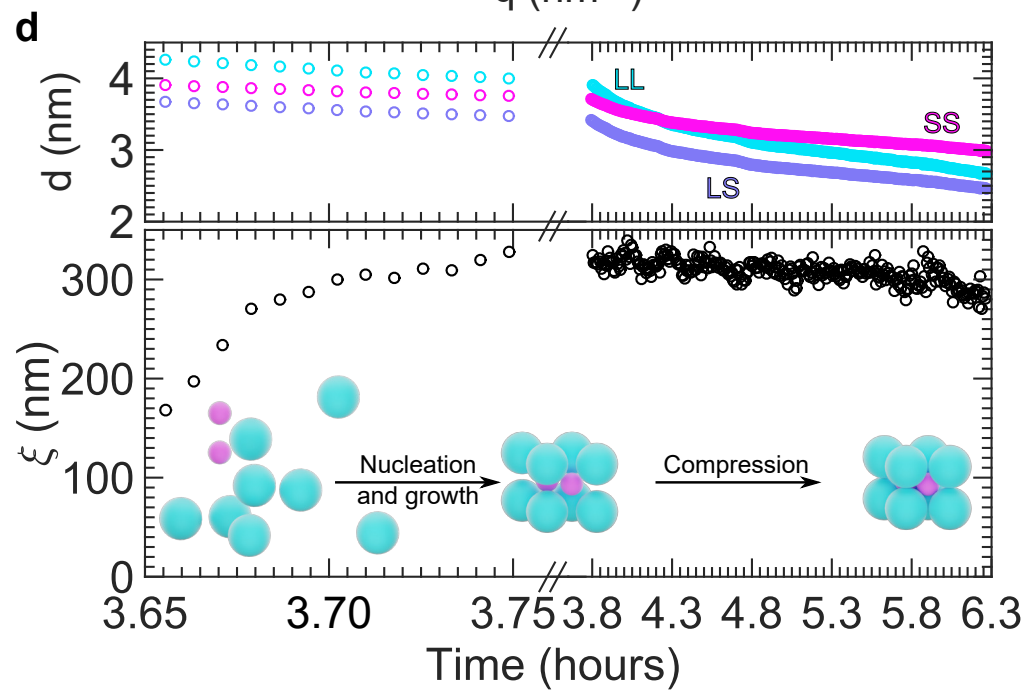
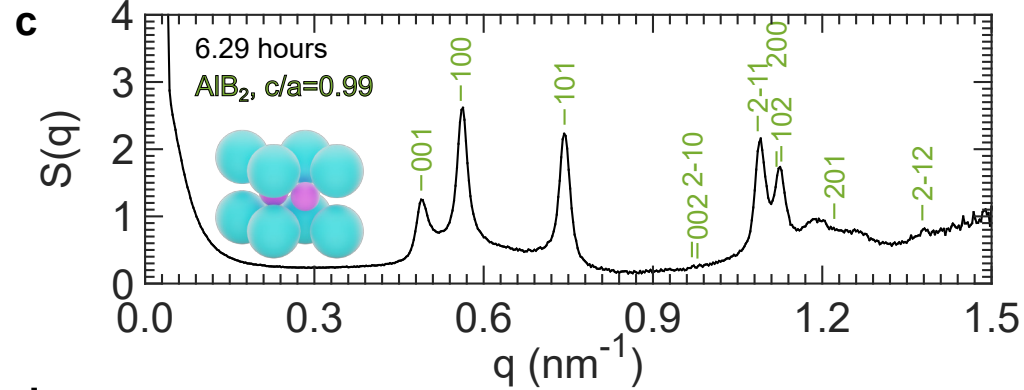
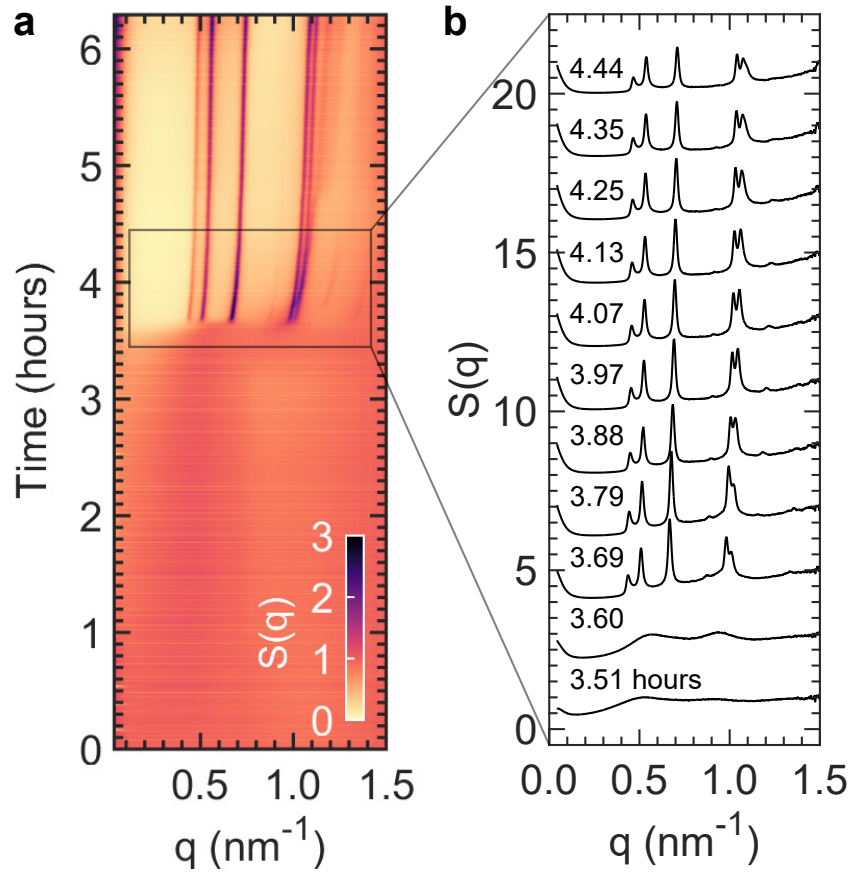
914 117 Stukowski, A. Visualization and analysis of atomistic simulation data with OVITO—the  
915 Open Visualization Tool. *Modelling and Simulation in Materials Science and*  
916 *Engineering* **18**, 015012, doi:10.1088/0965-0393/18/1/015012 (2009).

917 118 Adorf, C. S., Dodd, P. M., Ramasubramani, V. & Glotzer, S. C. Simple data and  
918 workflow management with the signac framework. *Computational Materials Science*  
919 **146**, 220-229, doi:<https://doi.org/10.1016/j.commatsci.2018.01.035> (2018).

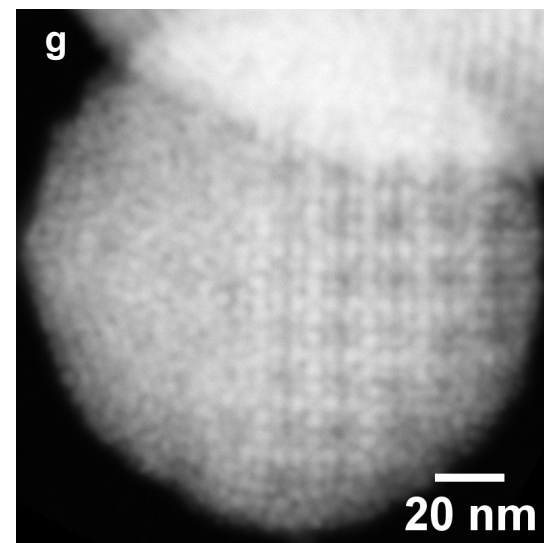
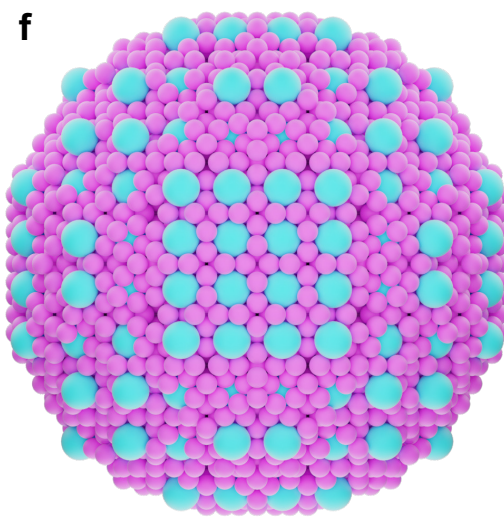
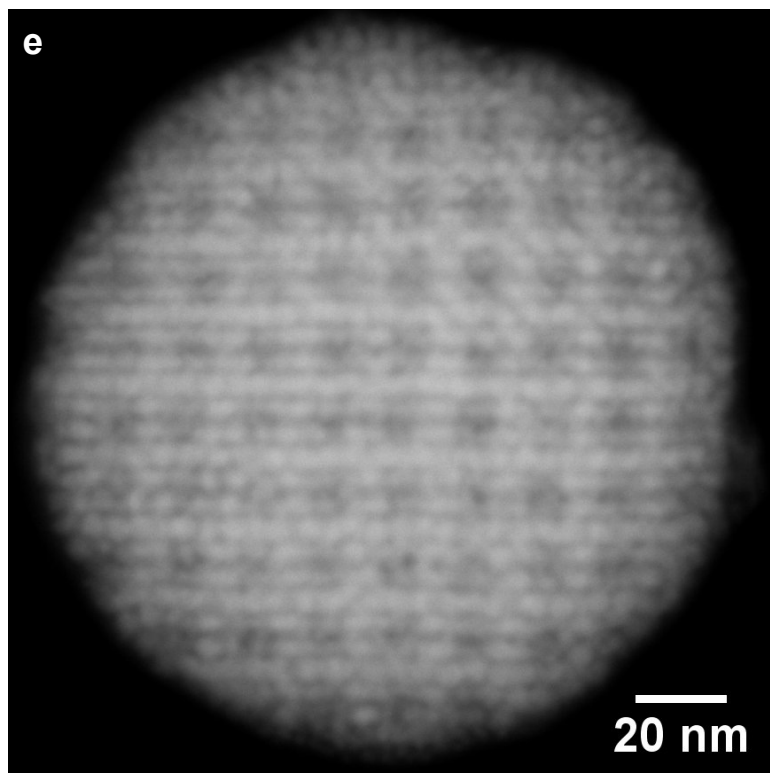
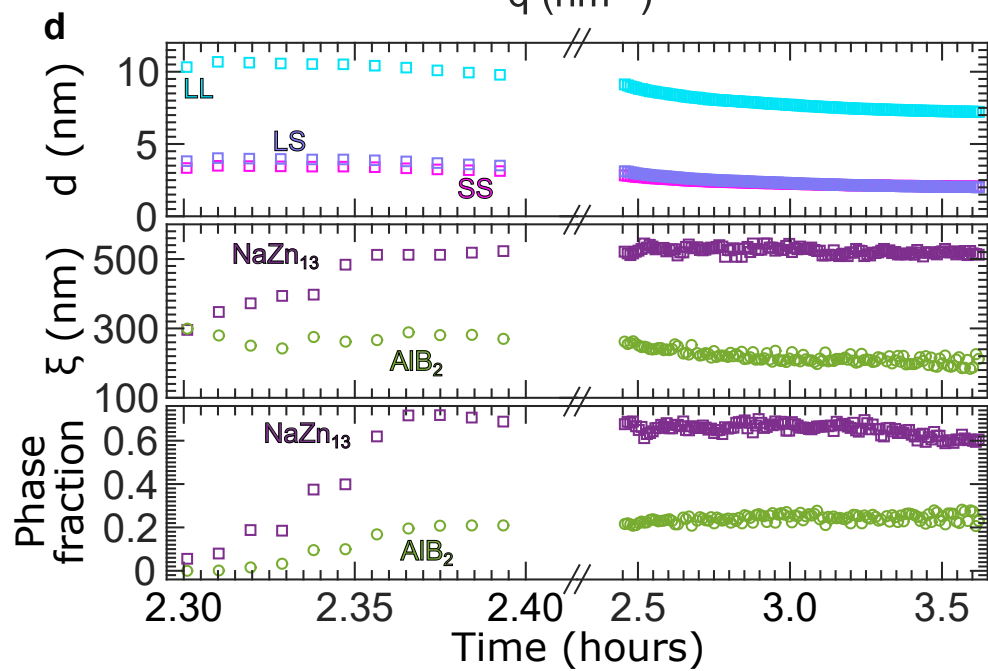
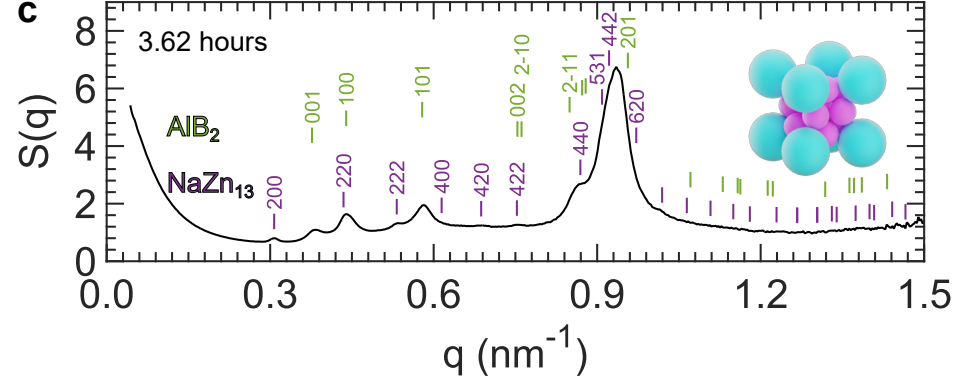
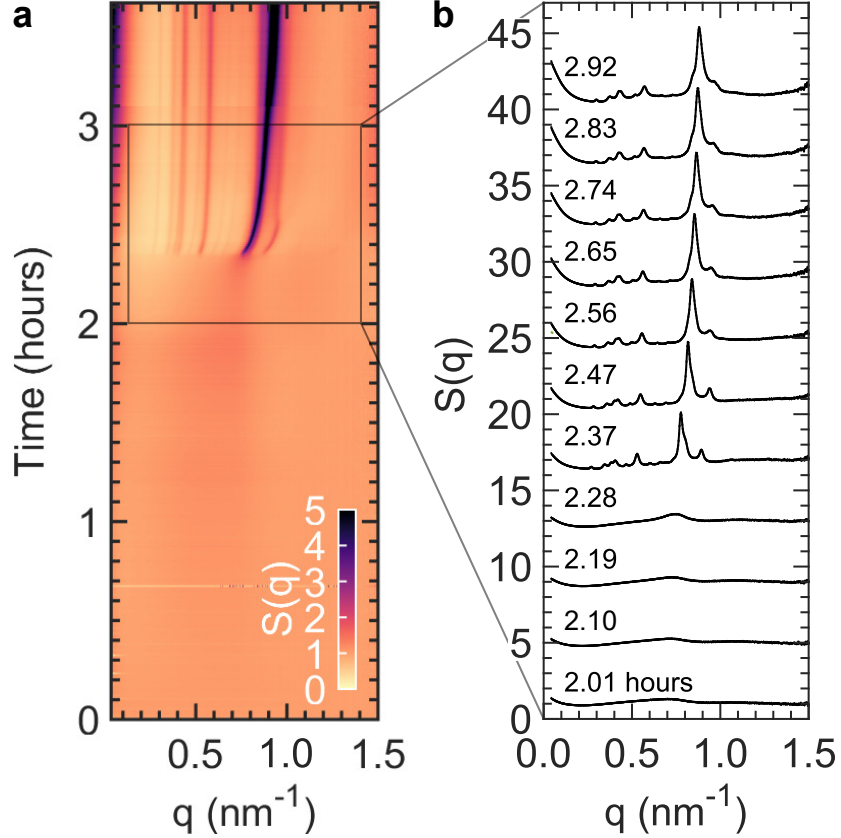
920 119 Ramasubramani, V., Adorf, C., Dodd, P., Dice, B. & Glotzer, S. in *Proceedings of the*  
921 *Python in Science Conference*.

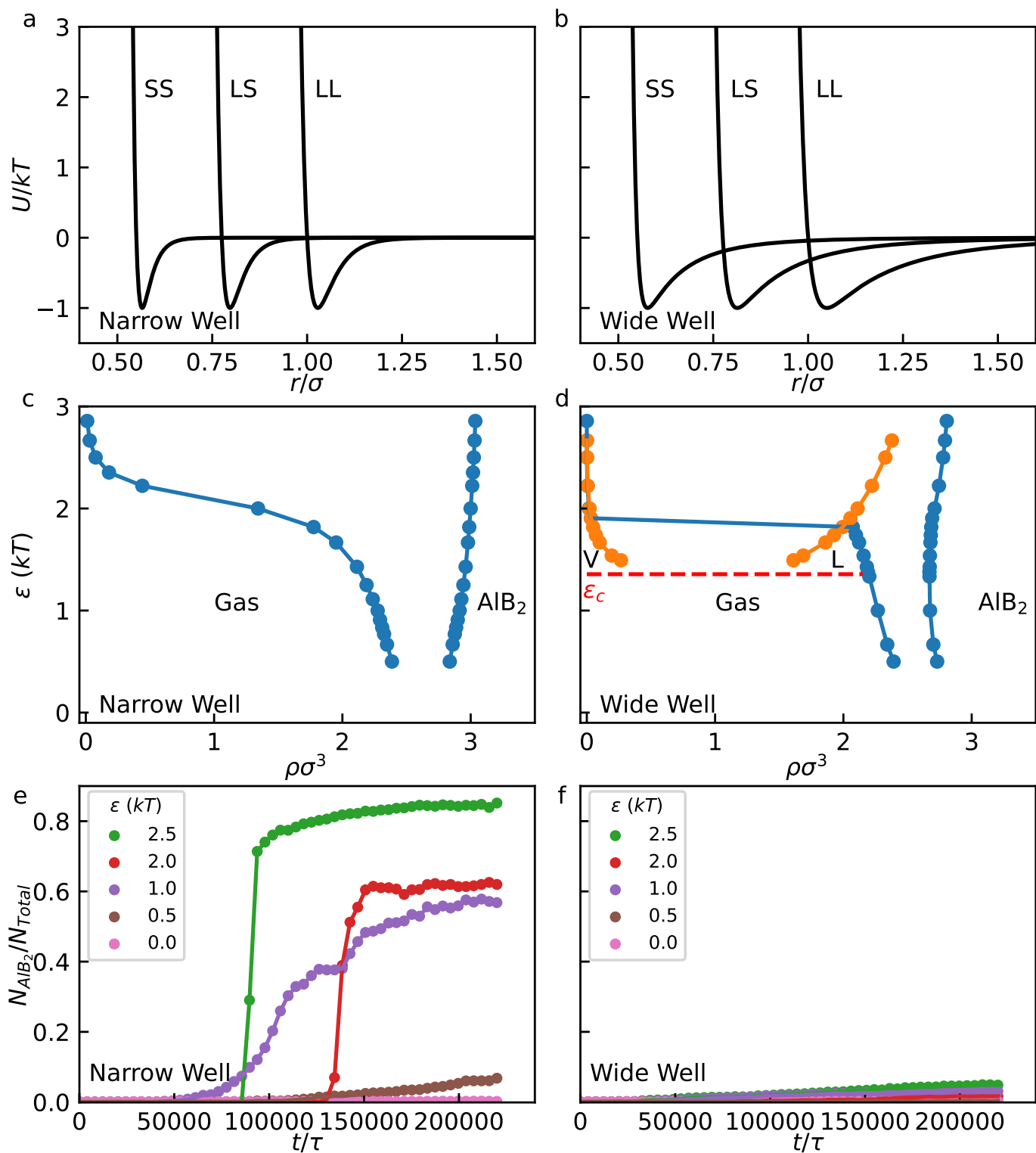
922 120 Towns, J. *et al.* XSEDE: Accelerating Scientific Discovery. *Computing in Science &*  
923 *Engineering* **16**, 62-74, doi:10.1109/MCSE.2014.80 (2014).

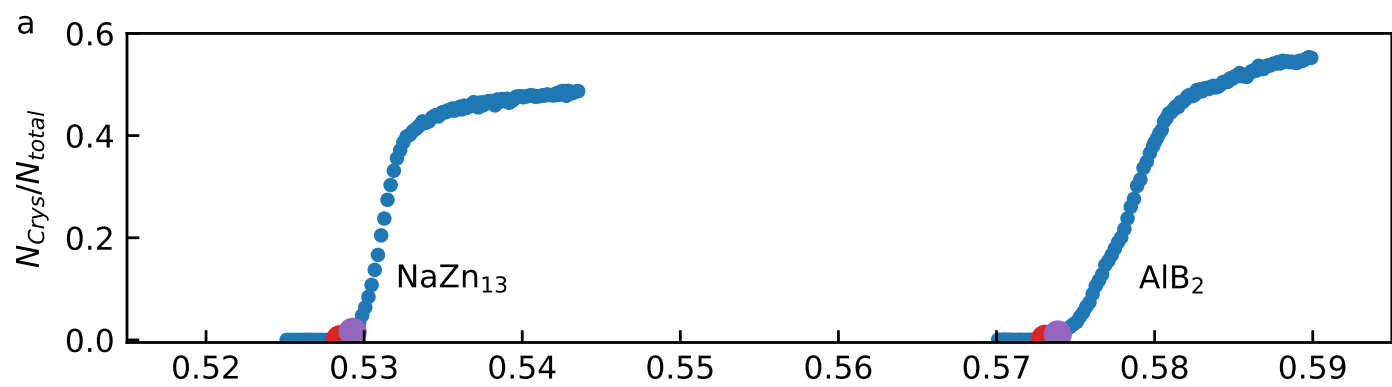
924



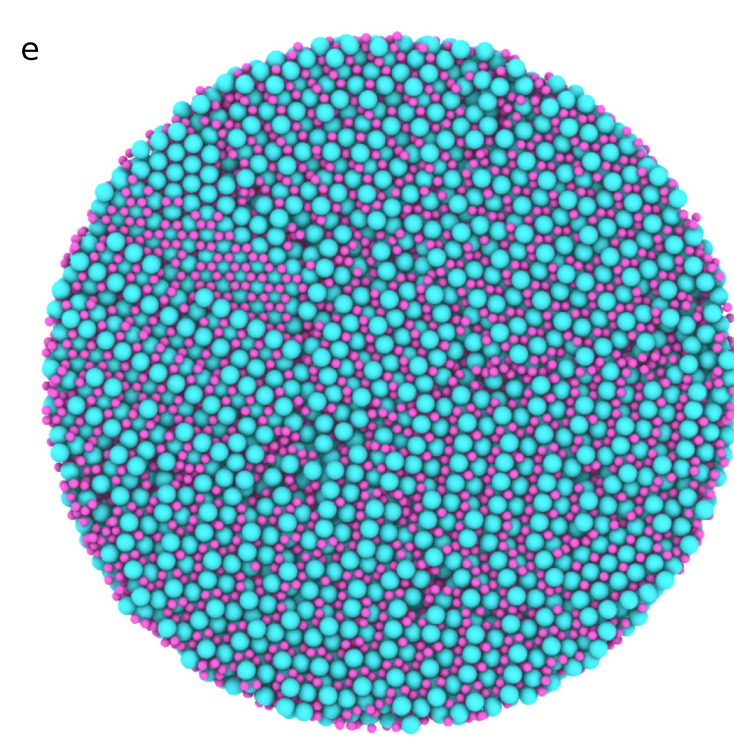
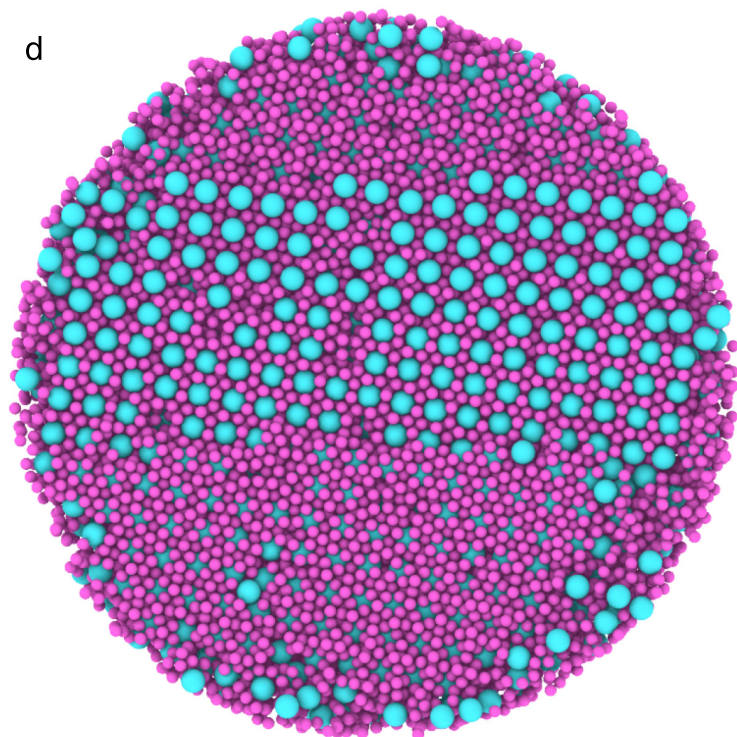
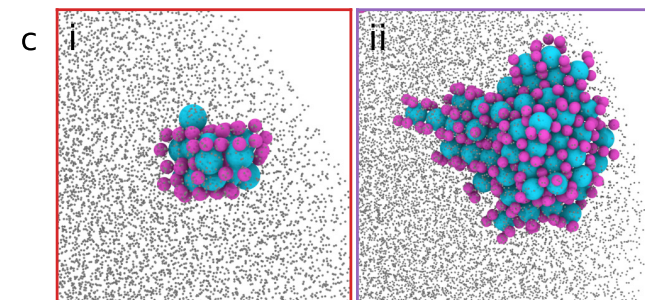
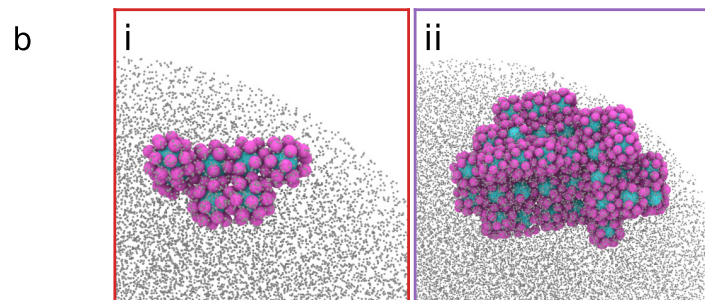






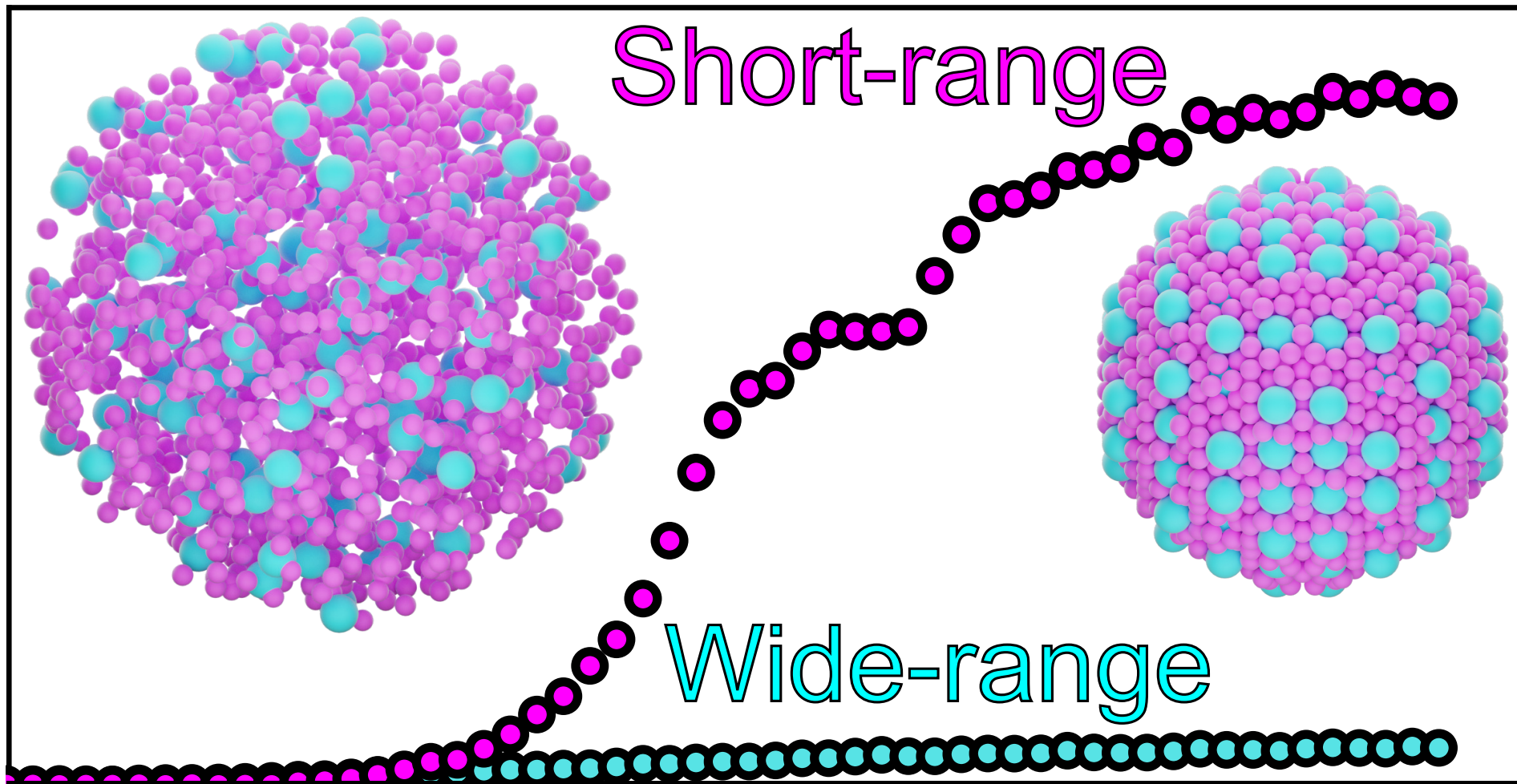


$\phi$





Crystallization



Assembly time